Coherent Raman Scattering Microscopy in Biology and Medicine

Chi Zhang, Delong Zhang, and Ji-Xin Cheng

Weldon School of Biomedical Engineering and Department of Chemistry,
Purdue University, West Lafayette, Indiana 47907; email: jcheng@purdue.edu

Keywords

Raman scattering, vibrational spectroscopy, biomedical imaging,
multimodal imaging, clinical setting

Abstract

Advancements in coherent Raman scattering (CRS) microscopy have
enabled label-free visualization and analysis of functional, endogenous
biomolecules in living systems. When compared with spontaneous Raman
microscopy, a key advantage of CRS microscopy is the dramatic improve-
ment in imaging speed, which gives rise to real-time vibrational imaging of
live biological samples. Using molecular vibrational signatures, recently de-
veloped hyperspectral CRS microscopy has improved the readout of chemi-
cal information available from CRS images. In this article, we review recent
achievements in CRS microscopy, focusing on the theory of the CRS signal-
to-noise ratio, imaging speed, technical developments, and applications of
CRS imaging in bioscience and clinical settings. In addition, we present
possible future directions that the use of this technology may take.

Contents

1. INTRODUCTION

The Raman scattering phenomenon was discovered in the 1920s and named after C.V. Raman (1). It is an inelastic light-scattering process that can be used to probe intrinsic molecular vibrations. The wide application of Raman spectroscopy was greatly facilitated by the invention of the laser source (2). Raman spectra reflect signatures of molecular vibrations, which provide an ideal contrast for chemical imaging in biology and medicine. Imaging systems using laser-excited Raman spectroscopy for chemical or tissue analysis are termed Raman microscopes or microprobes (3, 4). State-of-the-art Raman microscopes have a typical imaging speed of several seconds per line, or minutes per image (5, 6). Such speed is insufficient for real-time imaging of living specimens. Additionally, Raman microscopy suffers from interference from fluorescence background.

These difficulties have been overcome by recent advances in coherent Raman scattering (CRS) microscopy, which is based on either coherent anti-Stokes Raman scattering (CARS) or stimulated Raman scattering (SRS) (7, 8). CARS is a parametric process in which input and output photons exchange energy but the quantum state of the molecules is left unchanged (that is, in the ground state) after the nonlinear process. In CARS, the pump–probe beam (ω_p) and the Stokes beam (ω_S) interact with molecules in the specimen, generating an anti-Stokes beam, ω_{aS}, as shown in **Figure 1a**. A resonance occurs when $\omega_p - \omega_S$ is tuned to match the frequency of a Raman-active molecular vibration, Ω, which shows a peak in the CARS spectrum. The CARS signal is usually accompanied by a nonresonant background, resulting from nonlinear optical responses mediated through molecular virtual or electronic states, or both (9). The first CARS observation was documented in 1965 by Terhune et al. (10) at the Ford Motor Company. Since then, CARS spectroscopy has been developed into a powerful tool for monitoring the dynamics of chemical reactions, especially in combustion analysis (11, 12). In 1982, Duncan and coworkers (13) reported using the first CARS microscope. In 1999, Zumbusch et al. (14) demonstrated CARS imaging of
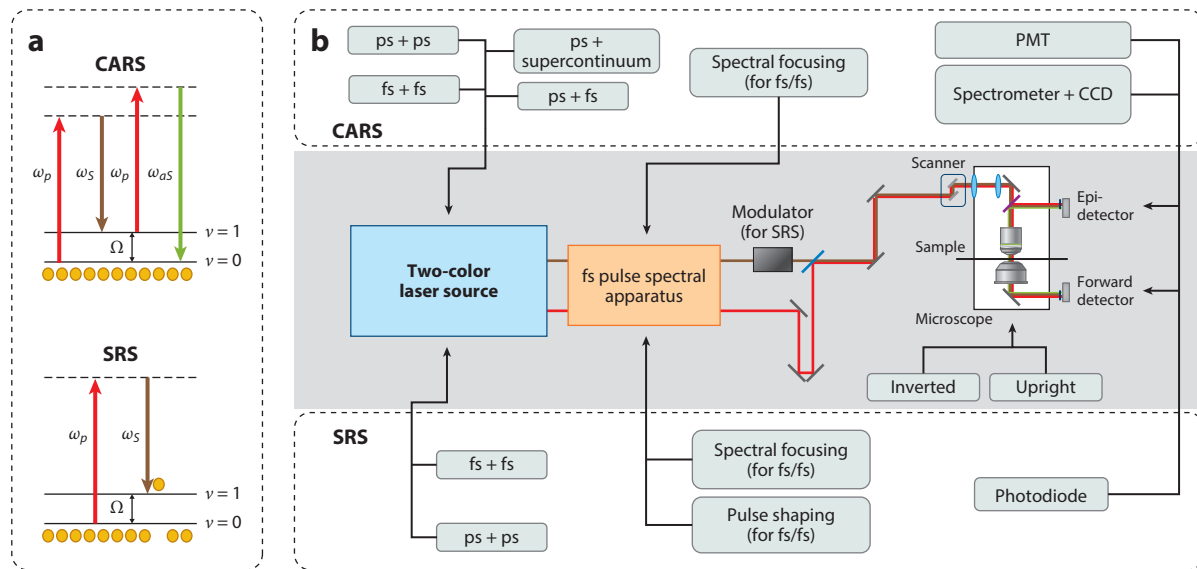
Figure 1

(*a*) Energy-level diagrams of the CARS and the SRS processes. (*b*) Instrumentation of CRS microscopy. (*Middle*, *shaded box*) Optical schematic diagram of CRS microscopy. (*Top*, *dashed box*) CARS imaging selections. (*Bottom*, *dashed box*) SRS imaging selections. Abbreviations: CARS, coherent anti-Stokes Raman scattering; CCD, charge-coupled device; CRS, coherent Raman scattering; fs, femtosecond pulse excitation; PMT, photomultiplier tube; ps, picosecond pulse excitation; SRS, stimulated Raman scattering; Ω, Raman-active molecular vibration; ω_{aS}, anti-Stokes beam; ω_p, pump–probe beam; ω_S, Stokes beam.

living cells with femtosecond (fs) pulses and a collinear beam geometry, which triggered the development of modern CARS microscopy. By exciting a single Raman band using picosecond (ps) lasers, Cheng et al. (15) showed that polarization CARS can discriminate the nonresonant background; they then developed high-speed laser-scanning CARS microscopy to image living cells (16). At the same time, epi-detected CARS microscopy was shown to minimize the detection of nonresonant signals (17), and later was used for in vivo video-rate imaging (18). On the theoretical side, a Green's function model was developed to interpret the radiation pattern of CARS from a 3D object (19). Multiplex CARS microscopy was an important development because it enabled the simultaneous detection of multiple Raman bands. It was first demonstrated in 2002 (20, 21) using a picosecond-pulsed laser synchronized to a femtosecond-pulsed laser. Quantitative multiplex CARS imaging was enabled by algorithms that extract Raman spectra from the CARS signal (22, 23). The strong signal in the C–H stretching region (2,800–3,100 cm^{-1}) has allowed CARS to image lipid-rich specimens, such as lipid bodies (24, 25) and myelin sheaths (26–28) (for reviews, see References 9 and 29–32). Additionally, CARS microscopy has been extended into the fingerprint region (500–1,800 cm^{-1}) (33–36).

Unlike the parametric CARS phenomenon, SRS is a dissipative process in which energy is transferred from input photons to molecular vibrations (**Figure 1a**). SRS results in a gain in intensity in the Stokes beam and a loss in intensity in the pump beam, denoted, respectively, as stimulated Raman gain (SRG) and stimulated Raman loss (SRL). Because the SRS signals appear at the same wavelength as the excitation lasers, optical modulation and phase-sensitive detection are generally used to extract the signal from the laser pulse train. Although the SRS phenomenon was first observed as early as 1962 (37), the development of SRS microscopy only started during the past decade. Ploetz et al. (38) demonstrated SRS imaging with a broadband low-repetition-rate

laser in 2007. The Xie lab (39) and others (40–44) developed single-color real-time SRS imaging with megahertz modulation of high-repetition-rate lasers. Hyperspectral SRS microscopy, which provides Raman spectral information at each pixel, was demonstrated by four groups at about the same time (45–48). Unlike CARS, SRS microscopy is free of the nonresonant background, and thus can provide high contrast for chemical content in biological imaging (for reviews, see References 49 and 50).

In the following sections, we review CRS microscopy by describing its signal-to-noise ratio (SNR) and imaging speed in theory, the most widely adopted instrumentation strategies, its major biological applications, the development of fiber laser sources, and recent efforts made to translate CRS microscopy to clinical use. We also discuss the outlook for the technology.

2. SNR AND IMAGING SPEED

In this section we discuss major noise terms in laser spectroscopy and compare the SNR in spontaneous Raman microscopy with that in CRS microscopy for a single vibrational frequency at a single image pixel. We show that the SNR determines the corresponding imaging speed of different techniques.

2.1. Major Noise Factors in Laser-Based Raman Microscopy

In an image, a pixel with meaningful information should be resolved from noise in the background. The ability to resolve a signal from noise fluctuations in a given time period defines the sensitivity of an imaging system. Such capability is usually evaluated using the value of the SNR. The signal is the mean value (μ) of the desired measurement; it is usually converted into root mean square voltage output of the detector. Noise is defined as the standard deviation (σ) of the measured value originating from any sort of random fluctuation in the laser source or detector. A generic definition of the SNR can be expressed as

$$ SNR = \frac{\mu}{\sigma} = \frac{V_s}{\sqrt{\sum_i V_i^2}}. \tag{1} $$

Here, V_s denotes the signal voltage, and V_i represents each type of noise voltage. The SNR is determined by both the signal level and the noise level. In order to resolve a signal from noise, an SNR greater than 1 is required. Longer signal integration times can increase the value of the SNR. The sensitivity of an imaging system ultimately determines the minimum signal-integration time and the maximum imaging speed.

Different Raman microscopic systems are based on different optical processes, use different detection schemes, and thus have different signal levels. However, generally they all share three noise sources, including shot noise, laser-intensity $1/f$ noise, and detector Johnson noise.

Due to the quantum nature of electrons, the statistical fluctuations in both the photocurrent (i_P) and the detector dark current (i_D) give rise to shot noise, which satisfies the following form after a photodetector (51):

$$ V_{shot} = \sqrt{2e\,(i_P + i_D)\,\Delta f} \cdot R_l = \sqrt{\frac{e\,(i_P + i_D)}{\Delta t}} \cdot R_l. \tag{2} $$

Here, e is the elementary charge, Δf is the detector bandwidth, which can be correlated to the signal-collection time constant Δt through $\Delta f = 1/(2\Delta t)$, and R_l is the load resistance. Generally, i_D is much weaker than i_P.

Laser-intensity $1/f$ noise has an unclear origin and may significantly affect CRS imaging. Laser relative intensity $1/f$ noise (RIN) is frequency dependent, and is typically expressed as noise power

density using a logarithmic scale [unit, decibels relative to the carrier/frequency (dBc/Hz)]. To convert this variation into a percentage and then into a voltage, we have

$$V_{1/f} = \sqrt{10^{\sigma_{RIN}/10}\Delta f} \cdot GPR_l = \sqrt{\frac{10^{\sigma_{RIN}/10}}{2\Delta t}} \cdot GPR_l. \tag{3}$$

Here, G is the responsivity [unit, ampere/watt (A/W)] of the detector, and P is the average light power detected by the photodetector. The noise power density (σ_{RIN}) is a function of the measurement frequency, and is approximately proportional to $1/f$.

Johnson noise is caused by the thermal agitation of electrons in a resistor. It can be considered blackbody radiation emitted from the resistor into the circuit, and thus, it is temperature dependent (52):

$$V_J = \sqrt{4k_B T R_l \Delta f} = \sqrt{\frac{2k_B T R_l}{\Delta t}}. \tag{4}$$

Here k_B is the Boltzmann constant and T is the temperature in Kelvin.

2.2. SNR in Spontaneous Raman Microscopy

Spontaneous Raman microscopy usually requires measurement of the entire broadband Raman spectrum. Therefore, signals are usually detected using highly sensitive arrays of avalanche photodiodes or charge-coupled devices (CCDs). The output voltage generated by a Raman transition signal can be expressed as

$$V_{Raman} = i_{Raman} R_l = N\sigma \left(\frac{P}{A}\right) GsR_l. \tag{5}$$

Here, N is the number of molecules probed by the laser, σ is the Raman scattering cross-section of each molecule for a specific Raman band, P is the input laser power, A is the beam area at focus, R_l is the load resistance, G is the responsivity of the detector, and s is the efficiency of signal collection. For a strong Raman band, a typical value for σ is 10^{-29} cm^2 (53). Using a water-immersion objective lens with a numerical aperture equal to 1.1 for excitation-beam delivery and signal collection, we could have $A \approx 0.09\ \mu m^2$ and $s \approx 20\%$, under tight-focusing conditions. Assuming that in the focal volume the number of molecules being probed is $N = 10^9$, and choosing typical experimental values, such as $P = 100$ mW, $G = 100$ A/W (for an avalanche photodiode), and $R_l = 100$ kΩ, we could obtain $i_{Raman} \approx 2 \times 10^{-11}$ A, and $V_{Raman} \approx 2 \times 10^{-6}$ V.

The detector for spontaneous Raman spectroscopy is usually cooled to reduce the dark current. Assuming $T = 200\ K$, $i_D \approx 10^{-19}$ A at 200 K, and a laser RIN power density of approximately -110 dBc/Hz, the three noise terms for spontaneous Raman spectroscopy can be calculated to be

$$V_{shot,Raman} \approx \sqrt{\frac{ei_{Raman}}{\Delta t}} R_l \approx \frac{2 \times 10^{-10}}{\sqrt{\Delta t}},$$

$$V_{1/f,Raman} = V_{Raman}\sqrt{\frac{10^{\sigma_{RIN}/10}}{2\Delta t}} \approx \frac{4 \times 10^{-12}}{\sqrt{\Delta t}},$$

and

$$V_{J,Raman} = \sqrt{\frac{2k_B T R_l}{\Delta t}} \approx \frac{2 \times 10^{-8}}{\sqrt{\Delta t}}.$$

These values show that when the detector works at 200 K, Johnson noise is the major factor limiting the SNR in spontaneous Raman spectroscopy. Under the previously mentioned experimental condition, $SNR_{Raman} \approx V_{Raman}/V_{J,Raman} \approx 100\sqrt{\Delta t}$. In this case, in order to achieve an

$SNR_{Raman} = 100$, the signal-integration time (Δt) needs to be approximately 1.0 s. Effective ways to improve the speed of signal collection include increasing the input laser power, increasing the number of molecules under detection, improving the efficiency of signal collection, reducing the detector's temperature, and using more sensitive detectors and higher load resistance. However, the imaging speed of modern Raman microscopy is still too slow to capture dynamics in living biological samples. CRS microscopy has overcome this problem by offering much higher sensitivity and faster imaging speed.

2.3. SNR in CARS Microscopy

The CARS signal can be derived from the following wave equation (see Reference 8):

$$\frac{dE_{aS}}{dz} = \frac{3\pi i}{n_{aS}\lambda_{aS}}\chi^{(3)}E_p E_S^* E_p. \tag{6}$$

Here E_{aS}, E_S, and E_p are optical field amplitudes of, respectively, the CARS signal, the Stokes beam, and the pump–probe beam. Also, z is the effective distance of the nonlinear process (the axial length of the excitation volume) along the laser-propagation direction; i is the imaginary unit; λ_{aS} is the wavelength of the CARS signal; and n_{aS} is the refractive index of the material at CARS signal wavelength. Additionally, $\chi^{(3)}$ is the third-order nonlinear susceptibility of the material, which is a function of molecular number density (or concentration), molecular orientation, and the third-order hyperpolarizability of each molecule (54). Using the definition of optical intensity $I = 0.5\sqrt{\varepsilon_0/\mu_0}nE^2 \approx nE^2/753$ (ε_0, vacuum permittivity; μ_0, vacuum permeability; n, refractive index), and ignoring the depletion of laser intensity by the sample, the solution of Equation (6) gives

$$I_{aS} = b_{CARS}\left|\chi^{(3)}\right|^2 I_p^2 I_S, \tag{7a}$$

$$b_{CARS} = \frac{5\times10^7}{n_{aS}n_S n_p^2}\frac{z^2}{\lambda_{aS}^2}. \tag{7b}$$

Here, b_{CARS} is a constant in a certain experimental condition. Assuming $n_{aS} = n_S = n_p = 1.3$, $\lambda_{aS} = 0.6$ μm, and $z = 1$ μm, we can derive $b_{CARS} \approx 5\times10^7$. The above results are obtained with the assumption of plane–wave interactions for both the pump–probe and the Stokes beams in a forward signal-detection scheme, in which phase matching is completely satisfied within the axial focus (z). Under tight-focusing conditions, the Gouy phase shift could lead to an additional phase mismatch that could affect the coherence length of the CARS signal in forward detection (19). The coherence length is the length within which the input and CARS waves stay in phase ($<\pi$). Additionally, under an epi-detection scheme, the coherence length for the CARS signal is typically much shorter than z (31).

We can further define the average input power of pump and Stokes beams as P_p and P_S, respectively; the laser beam repetition rate, pulse width, and beam area at focus can be defined, respectively, as f_{rep}, τ, and A. The average laser power P and the peak intensity I of pulses satisfy: $P = IAf_{rep}\tau$. The photovoltage generated by the CARS signal could then be derived from Equation (7):

$$V_{aS} = i_{aS}R_l = P_{aS}Gs R_l = I_{aS}Af_{rep}\tau_{aS}Gs R_l$$
$$= b_{CARS}\left|\chi^{(3)}\right|^2 I_p^2 I_S \cdot Af_{rep}\tau_{aS}Gs R_l \cdot q = b_{CARS}\left|\chi^{(3)}\right|^2\frac{P_p^2 P_S}{(Af_{rep})^2}\cdot\frac{\tau_{aS}}{\tau_p^2\tau_S}Gqs R_l. \tag{8}$$

Here τ_{aS}, τ_S, and τ_p are the pulse widths of, respectively, the CARS signal beam, the Stokes beam, and the pump–probe beam. Also, G is the responsivity of the detection system, and s is the

signal-collection rate. In CRS, the value of s could be close to 1 since the signal is directional and can be effectively collected by the detector. The term q represents the spectral and temporal match between the pump–probe and the Stokes beams, which equals 1.0 when the two beams have identical spectral and temporal widths. A mismatch in the frequency and time domains of the two beams would lead to $q < 1$.

The CARS signal is usually a combination of Raman transition ($\chi_R^{(3)}$) and a non-Raman-specific nonresonant contribution ($\chi_{NR}^{(3)}$). Third-order nonlinear susceptibility probed by CARS satisfies $|\chi^{(3)}| = |\chi_{NR}^{(3)} + \chi_R^{(3)}|$. In many cases, a strong nonresonant signal could severely distort Raman peaks (9). Such a nonresonant effect could also become overwhelming when the concentration of molecules that undergo a Raman transition is low, such as in a dilute solution.

To estimate the value of V_{aS}, we choose the typical experimental parameters $P_p = P_S = 5$ mW, $\tau_{aS} = \tau_S = \tau_p = 1$ps, $f_{rep} = 80$ MHz, $A = 0.09$ μm^2, $R_l = 50$ Ω, and $q = 1$. Furthermore, we set $s = 1$ by ignoring sample scattering and assuming that all signals are collected by the detector. Water has a nonresonant $\chi_{NR}^{(3)}$ at a level of 10^{-22} m^2/V^2 (8).

In a strongly resonant condition ($\chi_R^{(3)} \gg \chi_{NR}^{(3)}$), the nonresonant contribution has little effect when compared with the resonant term in a CARS spectrum, and $|\chi^{(3)}|^2 \approx |\chi_R^{(3)}|^2$. Here we assume that $\chi_R^{(3)} = 10\chi_{NR}^{(3)} = 10^{-21}$m^2/V^2. In single-frequency CARS, the signal is typically detected using a highly sensitive single-channel photomultiplier tube (PMT) with $G = 10^4$ A/W. Plugging these numbers into Equation (8) gives $i_{aS} \approx 1.2$ mA, and $V_{aS} \approx 60$ mV.

The CARS signal appears at a different frequency from the two input beams, and is spectrally separated for detection. The dark current of a PMT at room temperature is usually less than 10^{-8} A at normal working conditions, which is significantly lower than the CARS-signal photocurrent. Therefore, the shot noise in CARS arises mainly from the signal photocurrent i_{aS}:

$$V_{shot,\text{CARS}} \approx \sqrt{\frac{e i_{aS}}{\Delta t}} R_l \approx \frac{7 \times 10^{-10}}{\sqrt{\Delta t}}.$$

CARS microscopy usually does not utilize frequency modulation and demodulation technology as is used in SRS microscopy. The laser RIN power density is usually high (>-110 dBc/Hz) in the low-frequency range, making laser RIN an important noise factor in CARS. Considering the fluctuations of the pump, probe, and Stokes beams that give rise to the fluctuation in the CARS signal, a factor of 3 needs to be multiplied by the laser RIN percentage. Assuming $\sigma_{RIN} = -110$ dBc/Hz, we have

$$V_{1/f,\text{CARS}} = \sqrt{\frac{3 \times 10^{\sigma_{RIN}/10}}{2\Delta t}} V_{aS} \approx \frac{2 \times 10^{-7}}{\sqrt{\Delta t}}.$$

CARS experiments are usually performed at room temperature (T = 293 K). Therefore, Johnson noise can be calculated to be

$$V_{J,\text{CARS}} = \sqrt{\frac{2k_B T R_l}{\Delta t}} = \frac{6 \times 10^{-10}}{\sqrt{\Delta t}}.$$

The above results show that in this strongly resonant condition, the laser RIN is the factor that limits the SNR in CARS: $SNR_{CARS} \approx V_{aS}/V_{1/f,CARS} \approx 3 \times 10^5 \sqrt{\Delta t}$. To achieve an SNR equal to 100, a pixel dwell time of 0.1 μs is required. This speed allows the acquisition of a point-scanning image of 500 by 500 pixels within approximately 0.03 s. Experimentally, video-rate CARS imaging has been demonstrated to have a similar imaging speed (18).

For an isotropic material, $\chi^{(3)}$ is proportional to the number density of molecules. Therefore, when the sample concentration is reduced, the value of $\chi^{(3)}$ decreases. In this case, a longer signal-integration time is needed to achieve a similar SNR. For example, if in a strongly resonant

condition $\chi_R^{(3)} = 10^{-23}$ m^2/V^2, we can derive $V_{aS} \approx 6 \times 10^{-6}$ V, $V_{shot,CARS} \approx 7 \times 10^{-12}/\sqrt{\Delta t}$, $V_{1/f,CARS} \approx 2 \times 10^{-11}/\sqrt{\Delta t}$, $V_{J,CARS} \approx 6 \times 10^{-10}/\sqrt{\Delta t}$, and $SNR_{CARS} \approx V_{aS}/V_{J,CARS} \approx 10^4 \sqrt{\Delta t}$. In this case, Johnson noise is the dominating noise term. To achieve an SNR equal to 100, a 100 μs signal-integration time is required for each pixel.

In a weakly resonant condition ($\chi_R^{(3)} \ll \chi_{NR}^{(3)}$), the nonresonant term dominates the CARS spectrum and significantly distorts the resonant signal. In this condition, $|\chi^{(3)}|^2 \approx |2\chi_{NR}^{(3)}\chi_R^{(3)} + \chi_{NR}^{(3)2}|$, and one can choose to detect the mixed term $|2\chi_R^{(3)}\chi_{NR}^{(3)}|$ to derive the resonant contribution (known as heterodyne amplification). Assuming $\chi_R^{(3)} = 0.1\chi_{NR}^{(3)} = 10^{-23}$ m^2/V^2, we can derive $V_{aS} \approx 120$ μV. Since the detector sees both the resonant signal and the nonresonant background, and the latter is much stronger than the former, the shot noise is determined by the dominating nonresonant term $|\chi_{NR}^{(3)}|^2$, which gives $V_{shot,CARS} \approx 7 \times 10^{-11}/\sqrt{\Delta t}$. Additionally, we have $V_{1/f,CARS} \approx 4 \times 10^{-9}/\sqrt{\Delta t}$ and $V_{J,CARS} \approx 6 \times 10^{-10}/\sqrt{\Delta t}$. In this case, laser RIN is the noise factor limiting the SNR, and $SNR_{CARS} \approx V_{aS}/V_{1/f,CARS} \approx 3 \times 10^4 \sqrt{\Delta t}$. To reach an SNR equal to 100, at least 11 μs integration time for each pixel is needed. Furthermore, the imaging contrast would be largely reduced due to the strong nonresonant background.

2.4. SNR in SRS Microscopy

In SRS microscopy, one can choose to detect the SRL of the pump beam or the SRG of the Stokes beam. The sensitivity of these two schemes is similar, and here we choose to detect the SRL. The evolution of the pump-beam amplitude (E_p) in the SRS process can be derived from the wave equation (see Reference 8)

$$\frac{dE_p}{dz} = \frac{6\pi i}{n_p \lambda_p} \chi^{(3)} E_p E_S E_S^*. \tag{9}$$

Here E_S and E_p are the optical field amplitudes of, respectively, the Stokes and pump beams. The solution of this differential equation gives the signal intensity of the pump beam SRL:

$$\Delta I_p = -b_{SRS}\, \mathrm{Im}(\chi^{(3)}) I_p I_S, \tag{10a}$$

$$b_{SRS} \approx \frac{2.8 \times 10^4}{n_S n_p} \frac{z}{\lambda_p}. \tag{10b}$$

$\mathrm{Im}(\chi^{(3)})$ is the imaginary part of $\chi^{(3)}$, and it does not have the nonresonant contribution from $\chi_{NR}^{(3)}$. The value of $\mathrm{Im}(\chi^{(3)})$ for SRL at SRS resonance is positive (8). Here, b_{SRS} is a constant in a certain experimental condition. For example, assuming the reflective indices $n_S = n_p = 1.3$, the pump beam $\lambda = 0.8$ μm, and under the tight-focusing condition $z = 1$ μm, we have $b_{SRS} \approx 2 \times 10^4$. Similar to CARS, the SRS signal voltage can be derived to be

$$V_{SRS} = i_{SRS}R_l = \frac{1}{2}P_{SRS}GsR_l = \frac{1}{2}\left|\Delta I_p\right| Af_{rep}\tau_{SRS}GsR_l$$
$$= \frac{1}{2}b_{SRS}\,\mathrm{Im}(\chi^{(3)})I_p I_S \cdot Af_{rep}\tau_{SRS}GsR_l \cdot q = \frac{1}{2}b_{SRS}\,\mathrm{Im}(\chi^{(3)})\frac{P_p P_S}{Af_{rep}}\frac{\tau_{SRS}}{\tau_p \tau_S} \cdot GqsR_l. \tag{11}$$

There is a 1/2 factor in the equation because the SRS signal is generated only when the Stokes amplitude modulation is turned on (assuming a 100% modulation rate). The SRS measures the small variation in energy that is carried by the strong laser beam. Highly sensitive photodetectors, such as PMTs, cannot be used for SRS signal detection because directly measuring the laser beam would damage such detectors. A silicon photodiode is the ideal detector for an SRS signal. The typical responsivity of a photodiode is $G_{PD} = 0.5$ A/W. If we further assume that the lock-in amplifier gain is $G_{lock-in} = 100$, then $G = 0.5 \times 100 = 50$. Using the same parameters as in the

CARS calculation, and presuming $|\mathrm{Im}(\chi^{(3)})| = 10^{-21}\mathrm{m}^2/\mathrm{V}^2$ (a strong resonance), we can calculate $i_{SRS} \approx 1.7\,\mathrm{mA}$, and $V_{SRS} \approx 85\,\mathrm{mV}$.

If we choose to detect the SRL of the pump beam, all the pump power is dumped on the detector, which produces a strong shot noise. The photocurrent generated by the pump beam is $i_p = P_p G_{PD} qs \approx 2.5\,\mathrm{mA}$, which is significantly stronger than the photodiode dark current $i_D < 10^{-8}\,\mathrm{A}$. The corresponding photovoltage before lock-in amplification is $V_p = i_p R_l \approx 125\,\mathrm{mV}$. This gives the shot-noise voltage after lock-in amplification:

$$V_{shot,\mathrm{SRS}} \approx G_{lock-in}\sqrt{\frac{e i_p}{t}} R_l \approx \frac{10^{-7}}{\sqrt{\Delta t}}.$$

For the solid-state optical parametric oscillator (OPO) source typically used in SRS imaging, the laser RIN power density can reach $-150\,\mathrm{dBc/Hz}$ at the megahertz frequency range, where the modulation and demodulation are performed for SRS microscopy. This gives

$$V_{1/f,\mathrm{SRS}} = G_{lock-in}\sqrt{\frac{10^{\sigma_{RIN}/10}}{2t}} V_p \approx \frac{3 \times 10^{-7}}{\sqrt{\Delta t}}.$$

SRS signal detection is typically performed at room temperature. Therefore, the photodiode Johnson noise after lock-in amplification is

$$V_{J,\mathrm{SRS}} = G_{lock-in}\sqrt{\frac{2k_B T R_l}{t}} \approx \frac{6 \times 10^{-8}}{\sqrt{\Delta t}}.$$

From the above analysis, we find that when the laser RIN power density is as low as $-150\,\mathrm{dBc/Hz}$, the laser shot noise and RIN are at the same level, both slightly higher than the detector Johnson noise. Therefore, under the abovementioned condition, the total noise voltage can be calculated as

$$V_{noise,\mathrm{SRS}} = \sqrt{V_{shot,\mathrm{SRS}}^2 + V_{1/f,\mathrm{SRS}}^2 + V_{J,\mathrm{SRS}}^2} \approx 3 \times 10^{-7}/\sqrt{\Delta t}.$$

In this case, $SNR_{SRS} \approx V_{SRS}/V_{noise,SRS} \approx 3 \times 10^5 \sqrt{\Delta t}$. In order to achieve an SNR of 100, the signal-integration time needs to be approximately 0.1 µs. This speed is similar to that in the strongly resonant CARS condition, and has been demonstrated by video-rate SRS imaging (55).

If the laser source is not quiet enough at modulation frequency, e.g., with a RIN power density of $-120\,\mathrm{dBc/Hz}$, the RIN can exceed the shot noise and become the major noise issue in SRS microscopy. In this condition, the RIN voltage becomes $V_{1/f,SRS} \approx 9 \times 10^{-6}/\sqrt{\Delta t}$ and is the noise factor limiting the SNR. In order to have an SNR equal to 100, the integration time needs to be approximately 110 µs per pixel, which prevents fast acquisition of good-quality SRS images.

When the molecular concentration is lower, the value of $\mathrm{Im}(\chi^{(3)})$ becomes smaller, generating a lower SRS signal voltage at the same input laser power. Because the shot noise and the RIN in SRS do not depend on the signal level but rather on the power of the pump beam laser (in SRL detection), the SNR can be dramatically reduced, and thus, longer signal-integration time is necessary.

Overall, the signal level of CRS is much higher than that of spontaneous Raman scattering, thus allowing rapid vibrational imaging. Johnson noise limits the SNR in spontaneous Raman microscopy. And all three noise terms can affect the SNR in CRS microscopy, depending on the specific experimental conditions. In SRS, because the laser beam is detected, the shot noise is much higher than that in CARS. Utilizing a high-frequency modulation scheme, the laser RIN in SRS can be suppressed to the level of shot noise.

3. INSTRUMENTATION OF CRS MICROSCOPY

In this section we discuss the most widely adopted scheme for CRS microscopy: using two synchronized pulse trains on a laser scanning microscope, as summarized in **Figure 1b**. CARS and SRS usually happen simultaneously and thus can share the same laser source and microscope system. However, they utilize different signal-detection devices. Also, instead of using two beams to provide pump and Stokes pulses, single-pulse CARS microscopy (56) and single-beam SRS imaging (57) have been demonstrated using intrapulse excitation of broadband lasers. In addition to laser scanning, a wide-field CARS microscope has been developed using a dark-field objective lens (58).

3.1. Instrumentation Scheme for CARS Microscopy

A CARS microscope is generally composed of a dual-color laser source, a microscope, and a highly sensitive photodetector (**Figure 1b**). Picosecond-pulsed lasers have been proven theoretically and experimentally to be the optimal source in terms of the signal-to-nonresonant-background ratio for single-frequency CARS imaging (59). Twin picosecond laser systems with synchronized pulses were the major laser source in early CARS microscopy. Typically, the two beams are collinearly combined and sent to a laser-scanning confocal microscope with the pinhole removed, also known as a multiphoton microscope. An objective lens with a high numerical aperture is preferred, to maximize the power density on the sample for CARS signal generation. A PMT is used to collect signals at the CARS wavelength with a high-optical-density band-pass filter to block the laser beams. The use of electronically synchronized twin-laser systems suffered from temporal jitter between the two pulse trains. Laser pumped OPO was then adopted for high-speed jitter-free CARS imaging (60). An OPO is a parametric oscillator that is able to convert an input laser frequency into two tunable output frequencies with lower photon energies. Therefore, the output beams of an OPO are automatically synchronized with the input beam.

It is worth discussing the terms single-frequency (or single-color) and hyperspectral as used for CRS microscopy. Unlike spontaneous Raman microscopy, which acquires the whole Raman spectrum at each pixel, CRS microscopy usually focuses energy into a specific Raman shift to achieve a gain in signal level and imaging speed. Conventionally, CRS imaging was performed at a single Raman shift, a scheme which we term single-frequency CRS microscopy. Single-frequency CRS microscopy has limited chemical specificity, especially when the Raman bands of chemicals overlap. CRS microscopy that is performed over a continuous spectral range is called hyperspectral CRS microscopy. Depending on whether the spectral images are acquired in parallel or in serial order, hyperspectral CRS is generally categorized as multiplex (parallel) or wavelength (serial) scanning.

Multiplex CARS microscopy utilizes broadband and narrowband excitation beams to produce a CARS spectrum at each pixel that can be recorded by a spectrometer (20, 21). Unlike conventional CARS microscopy, which uses PMTs as photodetectors, multiplex CARS microscopy usually uses spectrometers and CCD arrays to collect the broadband spectrum generated at each pixel. The development of multiplex CARS microscopy has continued during the past decade (33, 61). The fastest spectral acquisition time is on the level of 3–5 ms (34). When compared with video-rate single-frequency CARS imaging, which has sub-microsecond pixel dwell time, this speed is largely limited by the CCD readout rate.

In addition to multiplex CARS microscopy, a few other methods have been developed for hyperspectral CARS microscopy. The first is to directly scan the wavelength of one narrowband excitation beam to match different Raman transitions. Automated wavelength tuning of the laser (62) and the OPO (63) have been demonstrated, with speeds that are much faster than the

image-acquisition speed in CARS. The second method is to properly chirp the two broadband excitation beams and tune the time delay between them, which is called spectral focusing. After chirping, the instantaneous overlapping of the two excitation pulses has a reduced-frequency bandwidth, thus improving the spectral resolution (64, 65). Tuning the time delay between the two chirped pulses can substantially change the overlapping difference in frequency, exciting different Raman shifts. Spectral focusing has been utilized by many groups for hyperspectral CARS imaging (66–69). The third method is to perform the Fourier transform on a time-resolved CARS trace (70, 71). This method can help remove the nonresonant background from samples and solvents in CARS imaging.

The direct readout of a CARS spectrum usually needs to be processed for quantitative analysis because the Raman signal is usually mixed with the nonresonant contribution of $\chi^{(3)}$, which shifts the peak position and distorts the shape of the Raman spectral line. To extract the actual Raman spectrum, the maximum entropy method (72) and the Kramers–Kronig transformation (73) have been used to quantitatively analyze hyperspectral CARS data. Alternatively, with the addition of a third laser beam, interferometric CARS can also produce actual Raman spectra (74). If the CARS spectral difference is significant enough, qualitative analyses can be made from hyperspectral CARS images without using complicated computations to directly distinguish chemicals (63).

3.2. Instrumentation Scheme for SRS Microscopy

The SRS imaging modality can be added to a CARS microscope by using an optical modulator, a photodiode detector, and a demodulator to extract the signal at the same laser wavelength (**Figure 1b**). A photodiode, instead of a PMT, is used to directly measure the excitation laser. Typically, the intensity of one beam is modulated at a high frequency (usually at the megahertz level) by an acousto-optic or electro-optic modulator, and a demodulator is used to extract the small variation in the intensity of the laser beam induced by SRL or SRG. The lock-in amplifier is the most widely used demodulator for SRS imaging. Alternatively, a lock-in-free SRS microscope has been demonstrated using a cost-effective resonant circuit (75).

The development of single-frequency SRS microscopy has allowed real-time chemical imaging based on a variety of isolated Raman bands. Hyperspectral SRS microscopy offers better chemical specificity, especially when overlapping Raman bands are present. Several approaches to hyperspectral SRS imaging have been demonstrated using dual picosecond pulses or dual femtosecond pulses. Using picosecond pulses, hyperspectral SRS imaging has been performed at multiple Raman transitions by tuning the laser wavelength over a continuous range (46). With the broad bandwidth provided by femtosecond pulses, hyperspectral SRS can be achieved more flexibly, without tuning the laser cavity. One method is based on intrapulse spectral filtering and uses a pulse shaper to filter and scan a narrow spectral component out of a broadband femtosecond spectrum (48, 76, 77). Similarly, spectral filtering coupled with a customized fiber amplifier also serves as a good hyperspectral laser source (45). Another method utilizes spectral focusing (47, 78), as discussed for hyperspectral CARS imaging (Section 3.1).

By recording a Raman spectrum at each pixel, multiplex SRS has strong potential for providing high-speed high-content biological imaging. Multicolor SRS was first demonstrated with parallel detection of three spectral channels using separate lock-in amplifiers (79). In order to increase the number of detection channels, Marx et al. (80) compared multichannel detectors that could be potentially used for SRS microscopy. Rock et al. (81) demonstrated recovery of the SRS spectrum after fast signal acquisition from a complementary metal-oxide-semiconductor (CMOS) array with a 20 ms integration time. The recent development of a multichannel lock-in detection scheme has shown promise for multiplex SRS imaging (82). The invention of a compact resonant amplifier

array has enabled multiplex SRS imaging with 32 μs pixel dwell time (83). The mapping of the composition of lipid droplets and retinoid metabolism in living systems has been facilitated with this multiplex SRS system (83).

4. APPLICATIONS USING CRS MICROSCOPY

During the past decade, CRS microscopy has been applied to study the metabolism of lipids, proteins, nucleic acids, and other metabolites in living cells and in simple model organisms. The CRS imaging of tissues has opened up novel applications for tissue biology and histopathology. In this section, we feature some examples that represent the vast accomplishments made recently. There are other reviews that can help achieve a broader understanding of the field (31, 50, 54, 84–87).
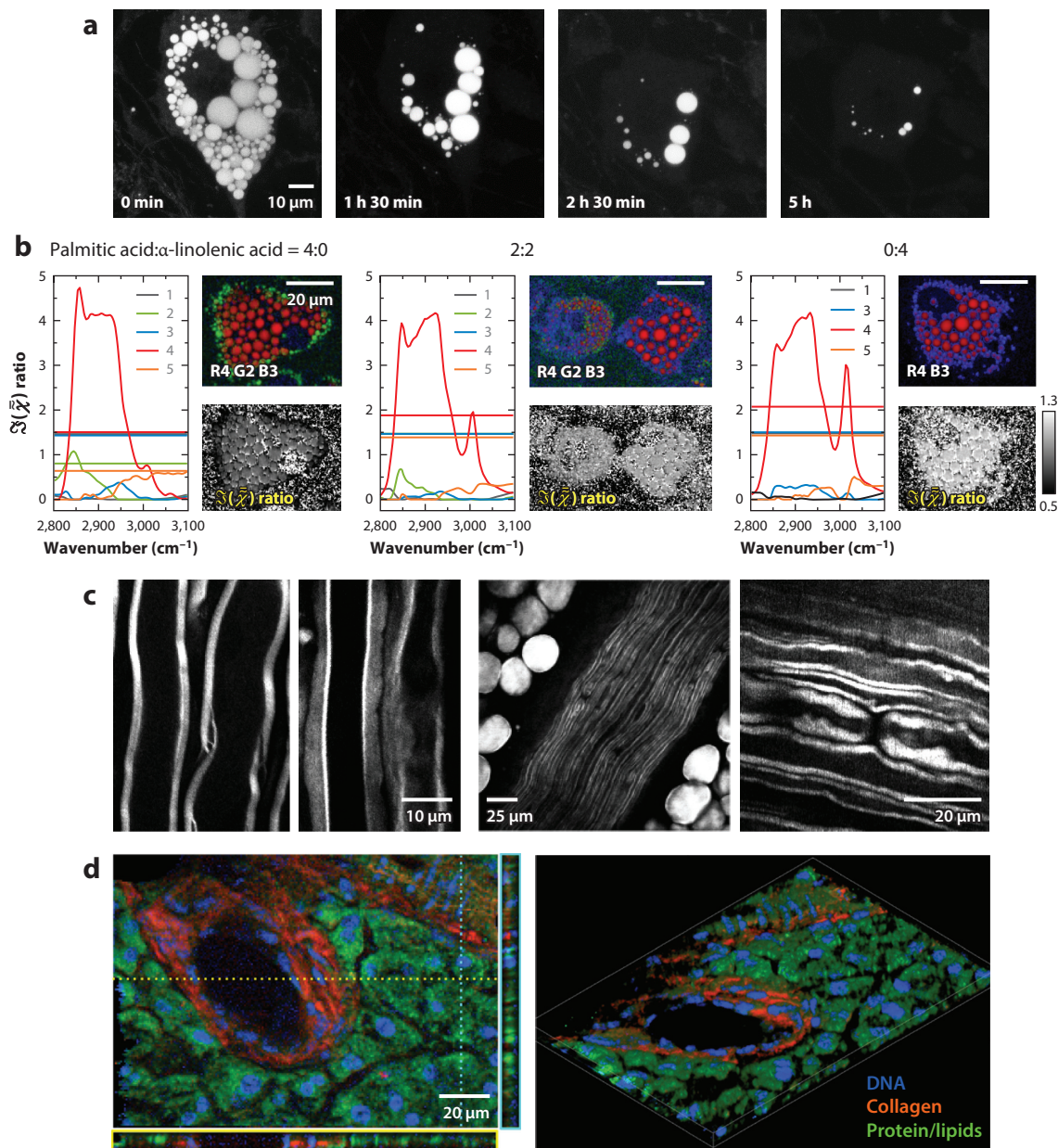
4.1. Applications Using CARS Microscopy

CARS microscopy has been extensively used for single-cell imaging (24, 25, 61, 88, 89). The strong CARS signal, especially in the C–H stretching region, provides unprecedented information about C–H rich contents, such as lipids and proteins at the subcellular level. For example, Nan et al. (24) performed CARS imaging of neutral lipid droplets in live fibroblast cells using CH_2 stretching vibrations. They also studied the behavior of lipid droplets during the 3T3-L1 cell-differentiation process (24). Paar et al. (88) studied the metabolism of intracellular lipid droplets during lipolysis using time-lapse CARS imaging. **Figure 2a** shows (from left to right) the gradual depletion of neutral lipid in 3T3-L1 adipocytes after stimulation with forskolin. In other work, reported by Le et al. (90), CARS was used to study the behavior of cancer cells in vitro and in vivo, and to evaluate the effect of a high-fat diet on cancer metastasis. CARS has also been employed to study circulating prostate tumor cells, which showed a sevenfold higher C–H intensity than did leukocytes (91). The uptake and breakdown of surfactant inside mammalian cells has been systematically studied using CARS microspectroscopy (92). The recent development of hyperspectral CARS imaging has led to promising results in the label-free chemical mapping of cellular components. For example, in a study published by Di Napoli et al. (35), human adipose-derived stem cells were fed with different ratios of palmitic acid (saturated) and α-linolenic acid (unsaturated). **Figure 2b** shows the hyperspectral CARS images of cellular components after this treatment and the corresponding CARS spectra, as well as the images of the resonance ratio $\Im(\bar{\chi})$ of peaks at 2,930 cm^{-1} (from the protein CH_3 group) and 2,855 cm^{-1} (from the lipid CH_2 group). The difference in lipid composition in these conditions was highlighted using this technique (35). A similar analysis in the fingerprint region has also been performed (35).

Caenorhabditis elegans has been used as a live test subject for CARS microscopy studies of fat storage and lipid metabolism (93–95). Hellerer et al. (93) used CARS microscopy to study the relation between genetic variations and metabolic pathways for lipid storage in living *C. elegans* by monitoring the detailed morphology of the organism and the geometrical arrangement of lipid droplets. Yen et al. (94) compared label-free CARS microscopy with a standard dye-labeled technique for imaging *C. elegans* and showed that CARS provides direct and noninvasive quantitative measurement of lipids, thus overcoming the many limitations of using the standard technique. The impact of genetic modification on *C. elegans*' neutral lipid storage and changes in the lipid unsaturation level were also studied using CARS (95).

At the tissue level, CARS has become a unique tool for studying tissue biology and diagnosing disease. An important application is the visualization of the myelin sheath in the central nervous system (26–28, 96, 97) and the peripheral nervous system (98, 99), which provides an effective way to study spinal cord injury and myelin disease ex vivo (**Figure 2c**, *left*) and in vivo (**Figure 2c**,

Figure 2

Applications using coherent anti-Stokes Raman scattering (CARS) microscopy. (*a, left to right*) Time-course CARS imaging of cellular lipid depletion in 3T3-L1 adipocytes induced by forskolin. Panel *a* adapted with permission from Reference 88. (*b*) CARS spectra with hyperspectral CARS images (*red, green, blue*) and images of the resonance ratio $\Im(\bar{\chi})$ (*grayscale*) of peaks at 2,930 cm^{-1} (from the protein CH$_3$ group) and 2,855 cm^{-1} (from the lipid CH$_2$ group) of human adipose-derived stem cells fed with palmitic acid and α-linolenic acid, showing the spatial distribution of different chemical components. Panel *b* adapted with permission from Reference 35. (*c, left*) Ex vivo CARS imaging of the myelin sheath in mouse spinal cord tissue; (*middle*) in vivo CARS imaging of parallel myelinated axons in the sciatic nerve and surrounding fat cells; (*right*) in vivo CARS imaging of the node of Ranvier in rat spinal cord. Panel *c* adapted with permission from (*left to right*) References 96, 98, and 28. (*d*) 3D broadband CARS imaging of a murine pancreatic duct showing distributions of DNA, collagen, and protein and lipids. Panel *d* adapted with permission from Reference 34.

middle and *right*). In **Figure 2c**, the myelin sheath, myelinated axons, and the node of Ranvier are highlighted (from left to right) with good contrast in CARS images. CARS microscopy has also been used to identify cholesterol crystals in the atherosclerotic tissue of diseased mice (46, 100) and humans (101). Recently, Camp et al. (34) demonstrated 3D tissue imaging using broadband CARS, which was capable of differentiating proteins and lipids, collagen, and DNA based on their distinctive spectra (**Figure 2d**). In their work, a broad Raman spectral window of 500–3,500 cm^{-1} was covered by hyperspectral CARS with excellent spectral resolution (<10 cm^{-1}). The heterodyne amplification of weak Raman transitions by the nonresonant background enabled high-quality CARS imaging of both the C–H stretching region and the fingerprint region. Furthermore, CARS has also been used to perform in vivo skin biopsy (102) and stain-free histopathology (103).

Additionally, CARS imaging has been used to study molecular orientation, such as the orientation of water molecules between phospholipid bilayers (104), the molecular orientation in hydrated and dry cellulose fibers (105), and the direction of lipid acyl chains in bilayer systems (106, 107).

4.2. Applications Using SRS Microscopy

The most important advantage of SRS microscopy compared with CARS microscopy is the absence of the nonresonant background, which could distort the Raman signal and complicate signal analysis. Similar to CARS, C–H stretching vibrations generate strong SRS signals, which allow for label-free SRS imaging of lipids and proteins in biological samples. The Xie group (39) used SRS to image the uptake of lipids and fatty acids in skin. Using SRS microscopy, Dou et al. (108) discovered the velocity-jump process in the trafficking of lipid droplets during early embryo development. Novel genetic regulators of fat storage have been discovered with the help of SRS imaging (109). In addition, SRS microscopy has moved to the fingerprint region (500–1,800 cm^{-1}). For example, Freudiger et al. (39) imaged skin uptake of dimethyl sulfoxide and retinoic acid using vibrations of S=O and C=C bonds at, respectively, 670 cm^{-1} and 1,570 cm^{-1}. Zhang et al. (110) have demonstrated the distribution of nucleic acid in live cells using Raman shifts at 785 cm^{-1} and 1,090 cm^{-1}. Saar et al. (111) studied the biomass conversion process in fresh plant tissue, focusing at 1,600 cm^{-1} and 1,100 cm^{-1} Raman bands for, respectively, lignin and cellulose.

At the single-cell level, SRS imaging has been used to image various cellular contents, such as lipids, proteins, and nucleic acid (78, 110–116). Fu et al. (78) observed in vivo cellular drug enrichment using a spectral focusing approach with hyperspectral SRS microscopy. The SRS images in **Figure 3a** show the enrichment of two drugs, imatinib (*left*) and nilotinib (*middle*),

Figure 3

Applying SRS microscopy. (*a*) Hyperspectral SRS imaging of drug enrichment in murine BaF3 cells. (*Left image panel*) SRS images at 1,305 cm^{-1} of a cell treated with 20 μM imatinib; (*middle image panel*) SRS images at 1,305 cm^{-1} of a cell treated with 20 μM nilotinib; (*right image panel*) SRS images at 1,305 cm^{-1} of a cell treated with dimethyl sulfoxide. (*Left spectral panel*) SRS spectra from the selected area of drug-treated cells; (*middle spectral panel*) SRS spectra from 100 mM drug solutions; (*right spectral panel*) SRS spectra from the cytosol of drug-treated cells and the control cell. (*b*) Protein degradation kinetics in HeLa cells imaged by SRS microscopy. The top and bottom panels correspond to time-lapse SRS images of ^{12}C-phenylalanine and ^{13}C-phenylalanine in cells, respectively. (*c*) In vivo, noninvasive SRS imaging of the nervous system of a *Xenopus laevis* tadpole. (*Left*) Membranes of single neurons in the optic tectum are lit up in the SRS image; (*right*) SRS imaging of the myelin sheath in the spinal cord. (*d*) Fingerprint SRS imaging of single cells (intracellular compartments) in whole *Caenorhabditis elegans*. Abbreviations: Daf-2, L2: *daf-2* mutant *C. elegans* at L2 stage; LROs: lysosome-related organelles; SRS: stimulated Raman scattering; WT N2, L2: wild-type N2 *C. elegans* at the L2 stage. Panels *a*, *b*, *c*, and *d* are adapted with permission from References 78, 115, 120, and 121, respectively.
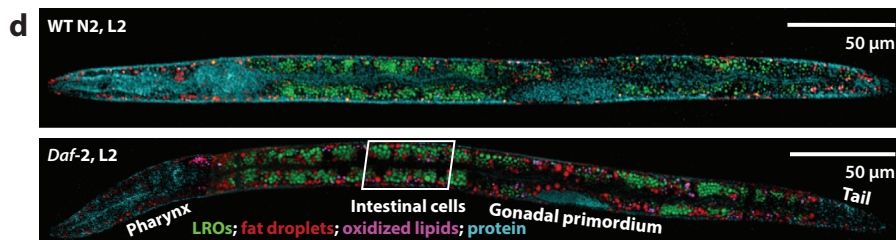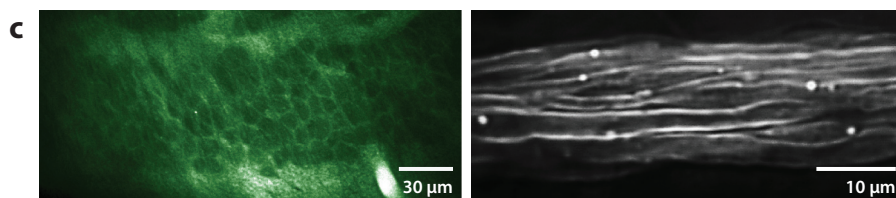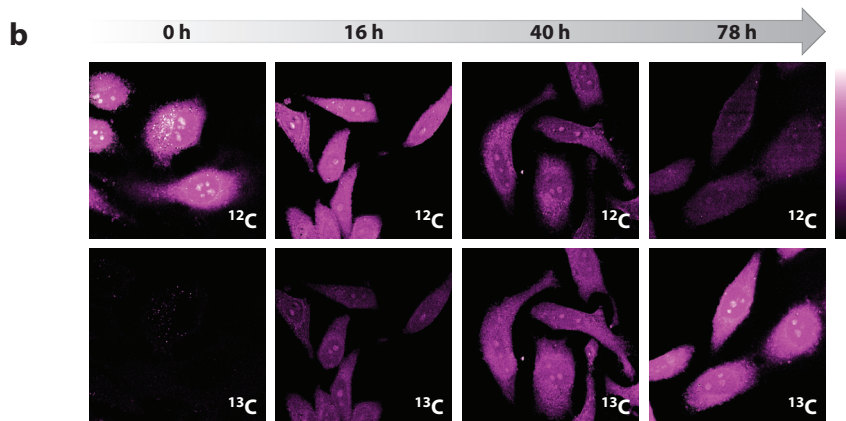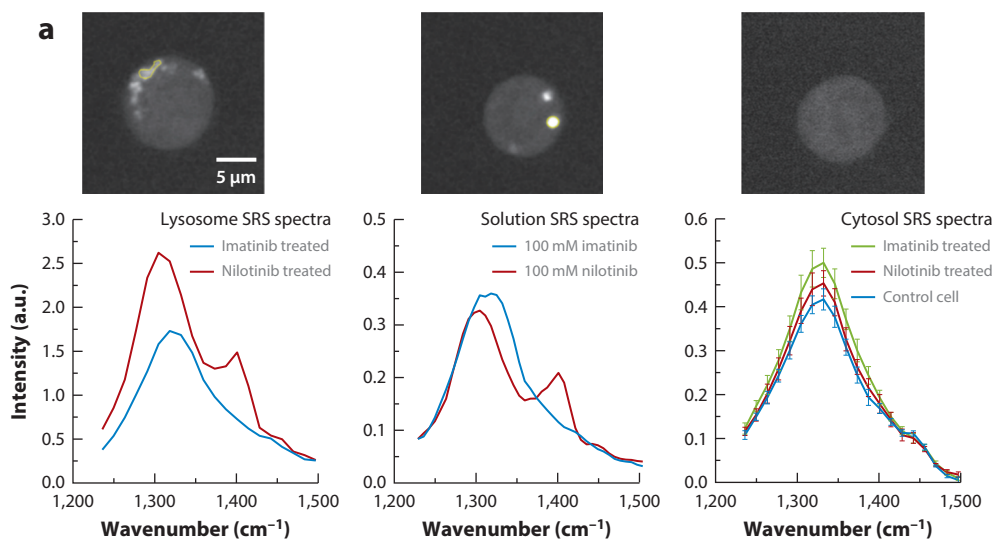
in murine BaF3 cells (a popular model cell system used for drug discovery), which is different from the control cells treated with only dimethyl sulfoxide (*right*). These drugs are effective Abelson tyrosine kinase inhibitors used to treat multiple cancers. The SRS spectra at selected locations (*left spectral panel*) show similar features to those of corresponding drugs in solution (*middle spectral panel*) but different from the cytosol area (*right spectral panel*), confirming the uptake and accumulation of drugs by the cells. This work further shows that the solubility and lysosomotropic properties of the drugs affect their cellular uptake and accumulation. Also, Raman tags, which usually have strong Raman bands separated from the intrinsic cellular Raman signal, have been developed for SRS imaging. Using SRS microscopy, Zhang et al. (42) studied cellular lipid uptake using treatment with deuterated fatty acids. Deuterated compounds have also helped visualize important metabolites in cells, such as protein and choline (112, 116, 117). Shen et al. (115) studied protein degradation in cells with carbon-isotope-labeled SRS imaging. In their work, endogenous and metabolically incorporated phenylalanine were marked by, respectively, carbon-12 (^{12}C) and carbon-13 (^{13}C). Time-lapse SRS images in **Figure 3b** show a significant decay in SRS intensity in the ^{12}C channel and an increase in the ^{13}C channel, indicating the gradual degradation of the old proteome and synthesis of a new proteome in cells. Recently, a few groups have reported the synthesis of Raman probes for imaging lipids, proteins, and DNA that are based on alkyne groups, which show a strong Raman shift at 2,120 cm^{-1} (113, 114), as well as isotope-edited alkyne groups (118). Rationally designed and synthesized phenyl-diyne cholesterol provides a strong Raman signal from the phenyl-diyne group at 2,254 cm^{-1}, which has enabled selective real-time mapping of cholesterol in living systems (119).

Many types of model organisms have been used in SRS microscopy. For example, Hu et al. (120) performed in vivo SRS imaging of single neurons in the tectum (**Figure 3c**, *left*) and myelin structures in the spinal cord (**Figure 3c**, *right*) in early-stage tadpoles. *C. elegans* has been extensively studied using SRS microscopy (42, 95, 109, 121). Wang et al. (109) compared CARS and SRS imaging of *C. elegans* and performed RNA interference screening based on the quantitative SRS imaging of lipids. Hyperspectral SRS has also been used in the fingerprint region to distinguish different chemical compositions in *C. elegans* (121). **Figure 3d** shows SRS images of a wild-type (*upper*) and a *daf-2* gene mutant (*lower*) *C. elegans* at the L2 stage, a stage of growth dominated by the development of the worm's intestinal cells. Different chemical components, including lysosome-related organelles, fat droplets, oxidized lipids, and proteins, were distinguished using hyperspectral SRS imaging together with *k*-means clustering and multivariate curve-resolution analysis. The *daf-2* gene is known to regulate the aging rate of *C. elegans*. This work shows that the *daf-2* mutant can significantly increase the storage of neutral fat and oxidized lipids in *C. elegans*.

SRS has been used in important applications in tissue biopsy as well. Wang et al. (77) showed the distributions of cholesterol crystals, lipids, and proteins in intact atherosclerotic arterial tissue. Yue et al. (122) used SRS microscopy to study human prostate cancer tissues at different stages, which showed increased storage of cholesteryl ester compared to normal prostate tissue. The Xie group reported in vivo SRS imaging of mouse skin (55) and brain tumor (123), and compared SRS images of various mouse organs with hematoxylin and eosin stained histopathological samples (124).

5. MULTIMODAL ANALYSIS USING A CRS MICROSCOPE

## 5.1. Multimodal Nonlinear Optical Imaging Using a CRS Microscope Platform

Microscopy based on different nonlinear processes can provide distinctive contrast for observing diverse endogenous biomarkers. Multiphoton fluorescence (MPF) microscopy can be used to light

up intrinsic biological fluorophores, such as NAD(P)H, elastin, and flavin. Second-harmonic generation (SHG) microscopy and sum-frequency generation (SFG) microscopy are more sensitive to molecules arranged without centrosymmetry, such as collagen fibers. CRS microscopy offers rich chemical information by imaging the intrinsic vibrational fingerprints of molecules. Multi-modal microscopy that combines several imaging modalities can bring together more molecular information and contrast to bring about a more profound understanding of biological samples. Different types of nonlinear microscopy can be integrated effectively because they all use ultra-fast lasers and laser-scanning technology for imaging. The CRS microscope is an ideal platform for implementing multimodal nonlinear optical imaging because it has two synchronized femtosecond or picosecond laser beams. There has been controversy over utilizing femtosecond or picosecond lasers for CRS microscopy (7). Although picosecond lasers may have better spectral resolution and cause less photodamage, femtosecond sources surpass picosecond sources with their extraordinary features, such as broadband frequency coverage for multiplex imaging, higher signal levels, and versatility in pulse shaping. Additionally, the conversion from femtosecond pulses to picosecond pulses is usually convenient yet irreversible. Another important advantage of using femtosecond sources for CRS microscopy is their capability for optimal integration with other nonlinear imaging modalities, such as SHG, SFG, and MPF, which require femtosecond pulses to generate sufficient signals.

Multimodal nonlinear microscopy has been developed and is based on synchronized lasers (125), single titanium (Ti) sapphire lasers (67), OPO systems (126), and fiber lasers (127, 128). With an appropriate design, various nonlinear optical signals can be collected simultaneously (85). Much work has been published about using multimodal nonlinear microscopy for various applications; these studies have been reviewed previously (85). Here, we provide a few examples to demonstrate the value of multimodal microscopy in biological imaging. **Figure 4a** is an image of a mammary gland from rat tissue; the image was collected using CARS and SHG microscopy (129). Adipocytes were delineated by the CARS signal (**Figure 4a**) at the C–H stretching frequency; collagen fibrils surrounding the adipocytes were highlighted using SHG (**Figure 4a**). Using this method, an obesity-induced increase in the size of lipid bodies in mammary gland adipocytes, and an increase in the collagen content of tumors, were observed, suggesting a breast cancer risk that is caused by obesity (129). **Figure 4b** is a multimodal nonlinear optical image of rabbit aortic tissue, which serves as a good example of combining several imaging modalities. In **Figure 4b**, the CARS signal marks lipids in adipose cells; the SHG signal defines the collagen fibers; and the two-photon excitation fluorescence (TPEF) signal gives excellent contrast to elastin in tunica media (67).

Multimodal nonlinear microscopy can also help characterize different types of atherosclerotic lesions in arteries (130). **Figure 4c–e** shows images from, respectively, CARS, SFG, and TPEF of a type-V porcine atherosclerotic plaque. The CARS image resolves a well-defined dense lipid core, and the SFG image shows severe disorganization in the surrounding collagen fibers. Together with the TPEF image pattern, the results show good agreement with analyses made using stain-based histology, indicating the potential of multimodal microscopy to provide label-free in vivo diagnosis of cardiovascular disease (130). **Figure 4f,g** shows SRS and SHG images of an intact aorta plaque from a diseased mouse. The combination of strong SRS and SHG signals indicates the structures with high molecular order, but the amorphous and noncrystalline nature of the other structures is indicated by their having only strong SRS signals. Further analysis showed that this combined technique allowed crystallized cholesterol to be distinguished from other structures in the tissue (46). These examples, together with contributions from other groups (101, 128, 131–137), highlight the merits of using multimodal nonlinear microscopy in biological applications.

Using the CRS microscope platform, multiple modalities have been developed to extend the capability of the system and its applications. For example, transient absorption (138, 139),
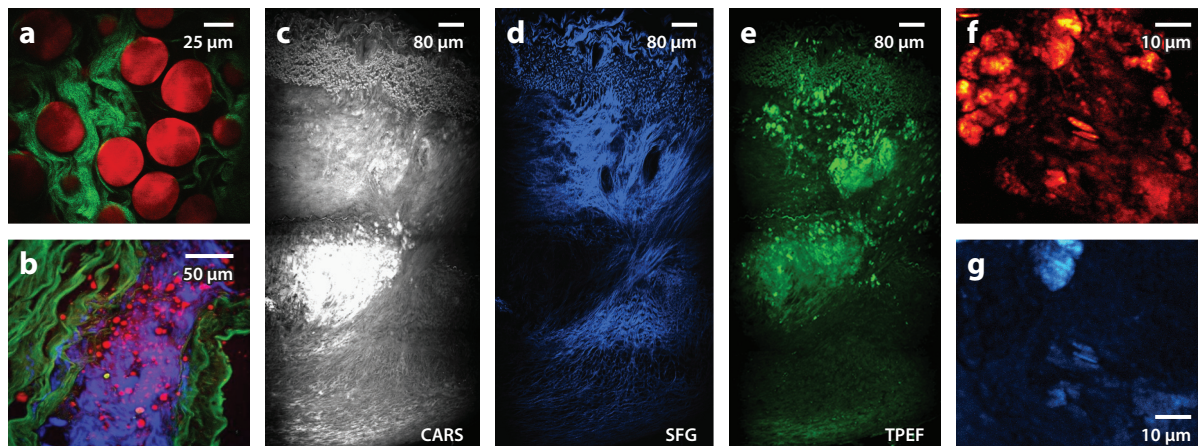
Figure 4

Multimodal imaging using a coherent Raman scattering (CRS) microscope. (*a*) Coherent anti-Stokes Raman scattering (CARS) (*red*) and second-harmonic generation (SHG) (*green*) multimodal image of a rat mammary gland showing, respectively, adipocytes and collagen fibrils. (*b*) CARS (*red*), SHG (*green*), and two-photon excitation fluorescence (TPEF) (*blue*) multimodal image of rabbit aortic tissue highlighting, respectively, lipid, collagen, and elastin compositions. (*c*) CARS, (*d*) sum-frequency generation (SFG), and (*e*) TPEF images of a porcine type-V atherosclerotic lesion section. (*f*) Stimulated Raman scattering and (*g*) SHG images of an intact mouse aortic plaque. All CRS images in this figure were collected at the CH_2 stretching frequency. Panels *a*, *b*, *c–e*, and *f–g* are adapted with permission from References 129, 67, 130, and 46, respectively.

multiphoton luminescence (140, 141), and four-wave mixing (142) modalities were developed based on CRS setups to provide high-contrast images of nanostructures. Stimulated emission microscopy and electronic enhanced four-wave-mixing microscopy enabled label-free imaging of chromophores (143–145). Photothermal lensing has been used to image nonfluorescent heme proteins (146) and the morphology of cortical microvasculature (147). The incorporation of fluorescence lifetime imaging microscopy with CARS has illustrated the potential of imaging molecular interactions in the vicinity of lipid-rich cellular structures (148).

5.2. Coupling Spontaneous Raman Spectroscopy with CRS Microscopy

Compared with spontaneous Raman microscopy, the gain in imaging speed in single-color CRS microscopy is accompanied by a loss of spectroscopic information. The most commonly used narrowband CRS microscope systems can image only a single wavelength at a time. By appropriately integrating CRS microscopy with spontaneous Raman spectroscopy, chemical information from samples can be read with both superb speed and detail. The Cheng group (149) developed a multimodal CRS and confocal Raman microspectroscopy platform, and showed its capability in differentiating chemical contents with small spectral differences in a biological sample. In this system, the CRS signal was collected forward using the microscope condenser, and the confocal Raman signal was collected backward using the objective lens. CRS can provide fast imaging of certain Raman transitions to light up locations of interest on a sample; then, confocal Raman microspectroscopy can further examine the specific locations to determine the chemical composition in detail. Using this method (149), lipid bodies in cultured cells and animal tissue were compared and the results suggested that the fat in adipocytes in live animals has a higher content of unsaturated fatty acid than that formed through de novo synthesis in cultured adipocyte 3T3-L1 cells (149). Le et al. (95) investigated lipid droplets in *C. elegans* and found that neutral lipid bodies in

C. elegans eggs possess higher unsaturation levels compared with those in the intestines. Slipchenko et al. (150) demonstrated the capability of this method to map active pharmaceutical ingredients and excipients in pharmaceutical tablets. Yue et al. (151) utilized this technique to study breast tissue polarity, an important feature related to mammary tumors. **Figure 5a** shows a CARS image of a section of mammary acinus collected at the CH_2 stretching frequency. **Figure 5b,c** shows magnified images of the purple and green squares in **Figure 5a**. Confocal Raman spectra in the C–H stretching range were collected at four locations in **Figure 5b,c**, including the apical membrane, basal membrane, cytoplasm, and nucleus, and the results are shown in **Figure 5d**. Distinct spectral features were found at different locations. These spectra could be further utilized to evaluate the lipid ordering and polarity of different locations in the tissue after spectral fitting (151). Additionally, with the help of this technology, the quantitative analysis of lipogenesis in cancerous tissues has been performed, and the accumulation of esterified cholesterol in the lipid bodies of prostate cancer cells was discovered (122). **Figure 5e–h** shows C–H stretching SRS images of, respectively, normal human prostate tissue, and low-grade, high-grade, and metastatic human prostate cancer. **Figure 5i** displays the corresponding Raman spectra of lipid bodies in **Figure 5e–h** plus a Raman spectrum of pure cholesteryl oleate. The Raman spectra of lipid droplets in these cancer tissues have similar features, and these features are significantly different from those of normal tissue but resemble those of cholesteryl oleate, suggesting there is a ubiquitous accumulation of cholesteryl ester in lipid bodies at all stages of prostate cancer. Further research has shown that depletion of cholesteryl ester could reduce the proliferation of cancer cells and suppress tumor growth (122). This Raman spectromicroscopy method has also been used to investigate spinal cord injury (152) and hepatic microvesicular steatosis (153).

6. FIBER LASER SOURCES FOR CRS MICROSCOPY

A more reliable and cost-effective CRS system would be more appealing to both scientists and doctors. The reliability and cost of a CRS setup are primarily determined by the laser source. Currently, most CARS or SRS imaging systems used in laboratories take advantage of state-of-the-art crystal-based solid-state lasers (such as Ti-sapphire lasers) and frequency-conversion systems (such as OPOs) that have excellent intensity stability and output pulse energy. However, these are costly, bulky, and sensitive to environmental change. The candidates expected to replace current laser systems are fiber lasers. Fiber lasers utilize fibers doped with rare earth elements as gain media and cost-effective diode lasers as pump sources to generate high-energy lasers with good quality. Due to the high surface-area-to-volume ratio of fibers, no bulky cooling component is necessary for high-power operation. Additionally, because light propagation in the laser cavity can be completely confined within the fiber media, environmental changes tend to have less effect on laser stability, and the need for precise spatial and optical alignment is largely eliminated. The absence of free-space optics in fiber lasers could also bring about the development of compact and miniature laser sources. Early on, the major obstacle to nonlinear microscopy using fiber lasers was the insufficient output of pulse energy, which ultimately required the involvement of amplification systems that increased the system's complexity. This problem was solved by the advancement of dissipative-soliton fiber lasers, which can output pulses of tens of nanojoules with a pulse width of hundreds of femtoseconds, thus reaching the energy level of solid-state crystal lasers (154–156). The corresponding peak power is strong enough for nonlinear microscopy (157, 158). Another approach is to utilize large-mode-area fibers as gain media, which leads to an output energy of up to 0.9 μJ (159), but this approach sacrifices some of the compatibility and flexibility of fiber lasers.

Compared with the emission bandwidths of a Ti-sapphire laser, those of most fiber media are narrow, resulting in a relatively poor wavelength tunability for fiber lasers. Accordingly,
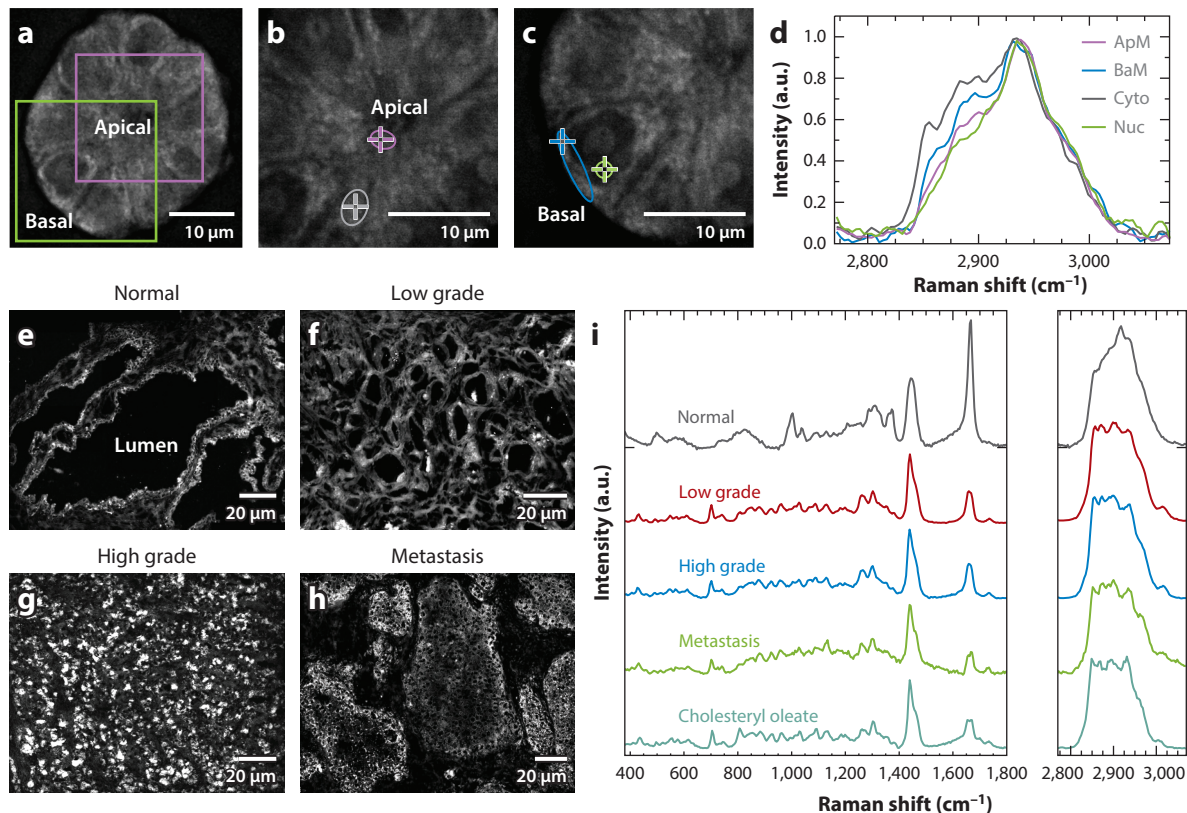
Figure 5

Coupling CRS imaging with spontaneous Raman spectroscopy. (*a–c*) C–H stretching CARS images of a mammary acinus with apical and basal poles. (*b,c*) Magnified areas of squares in panel *a* (*purple*, *green*). (*d*) Spontaneous Raman spectra of apical membrane (ApM, *purple*), basal membrane (BaM, *blue*), cytoplasm (Cyto, *gray*), and nucleus (Nuc, *green*) as indicated in panels *b* and *c*. (*e–h*) C–H stretching SRS images of human tissue from (*e*) normal prostate, as well as (*f*) low-grade, (*g*) high-grade, and (*h*) metastatic prostate cancer. (*i*) Spontaneous Raman spectra of lipid droplets in panels *e–h* and cholesteryl oleate. Panels *a–d* and *e–i* are adapted with permission from References 151 and 122, respectively. Abbreviations: a.u., arbitrary units; CARS, coherent anti-Stokes Raman scattering; CRS, coherent Raman scattering; SRS, stimulated Raman scattering.

fiber-based optical parametric amplifiers, OPOs, soliton-wave converters, and supercontinuum sources have been developed to broaden the spectral coverage, and these have been successfully applied to achieve high-quality CARS microscopy (34, 101, 127, 128, 160–163). However, problems occur when fiber lasers meet SRS imaging. In Section 2.4 we showed that the laser RIN can significantly affect the SNR in SRS microscopy. For most solid-state crystal lasers or OPOs, the laser RIN power density can reach as low as −150 dBc/Hz. However, fiber lasers are not as quiet as Ti-sapphire lasers; fiber-based frequency-conversion systems—including supercontinuum, optical parametric amplifiers, and OPOs—produce higher RINs, which limit the imaging speed of SRS microscopy. Balanced detection techniques can improve the SNR for fiber-laser-based SRS microscopy through noise subtraction, but it increases the complexity of the system (164, 165). Freudiger et al. (166) recently showed fast SRS imaging using fiber lasers and balanced detection, with a pixel dwell time of several microseconds, thus highlighting the potential of fiber lasers in SRS microscopy. Video-rate SRS microscopy has not been reported using a fiber source. Gaps

in stability, tunability, and performance remain when fiber lasers are compared with Ti-sapphire lasers for use in SRS microscopy. A fiber laser source with high output power, a low RIN, and a broad tuning range is expected to help push CRS imaging into clinical settings.

7. TOWARD CLINICAL APPLICATION

CRS imaging allows label-free visualization of endogenous contents in cells and tissues, which is valuable in clinical applications, such as disease diagnosis, histopathology, and during surgery. These applications drive the continual advancement of CRS technology toward the development of a robust, reliable, versatile, and user-friendly tool that can be used in clinical settings. Multiple groups are involved in moving the technology toward this goal. The major barriers include the reliability and cost of the system, as well as the penetration depth of light. Fiber lasers have the potential to significantly bring down the cost of the device and enhance its reliability. Recent, promising work has tailored fiber lasers toward clinical use (101, 128, 163, 166). The penetration depth of light restricts CRS microscopy to the study of the surface layers of samples. Therefore, most internal organs cannot be directly examined by CRS microscopy, and surgery is usually performed to help expose the location of interest. Samples obtained from surgery on animals or from human biopsy could be analyzed under a CRS microscope ex vivo to obtain chemical information with great ease and high speed. CRS microscopy has been performed on various biopsy sections, such as mouse retina (167), brain (34, 123), spinal cord (26), and liver (168), and on human breast glandular tissue (151), perivascular tissue (101, 128), the prostate gland, and cancerous tissue (122, 169). Technical improvements have allowed CRS microscopy to obtain more detailed information about structure and content for clinical purposes (101, 128). **Figure 6a** shows a frequency scatter plot from a high-resolution CARS image of tissue from a rabbit atherosclerotic lesion. This figure was plotted using spectral peaks at 2,850 and 2,924 cm^{-1}, corresponding to the C–H stretching of, respectively, the lipid CH_2 and protein CH_3 groups (101). From this figure, pixel contributions from these two channels were used to distinguish different chemical components in the image. **Figure 6b–d** shows a chemical map reconstructed from components 1, 2, and 3 in **Figure 6a**. With superior spectral resolution, these images allow the accurate identification of proteins and lipids in the sample.

In vivo tissue analysis using CRS microscopy has also been reported. The first in vivo CARS imaging was performed on mouse skin (18). Lipid structures in the 120-μm depth of skin were selectively lit up in detail by turning on the CH_2 stretching frequency (18). This work triggered other CRS-based skin research to understand, for example, drug penetration into skin (39, 170, 171) and skin disease (172). Furthermore, the use of integrated CARS, MPF, and SHG multimodal microscopy can illuminate the microscopic distributions of lipids, endogenous fluorophores, and collagen fibers (172, 173), providing invaluable insight for lab research on skin. Multimodal clinical imaging setups based on CARS have been established to provide label-free in vivo biopsy of skin (102, 174). A CARS exoscope has been developed to image skin in vivo (175). Although relatively new, SRS microscopy has been used extensively in skin research (39, 79, 170, 171, 176, 177). An SRS system customized for clinical use is expected.

In vivo SRS imaging of brain tumors has been performed on mice, with the help of craniotomy (123). In this work, two-color SRS microscopy was used to help delineate a brain tumor from normal brain tissue in vivo (123). It was found that the intensity ratio of CH_3 stretching at 2,930 cm^{-1} and CH_2 stretching at 2,845 cm^{-1} could be used to reflect the ratio of proteins to lipids in the brain; the ratio has a significantly higher value for tumors than for normal brain tissue. The in vivo experiment was performed on mice that had received xenografts of human glioblastoma
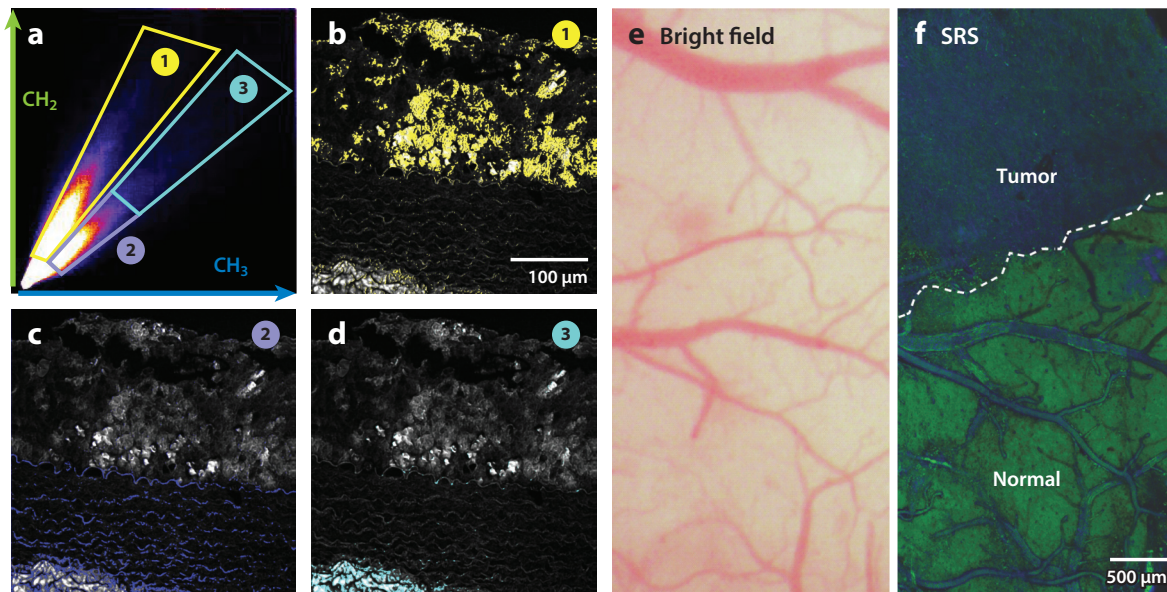
Figure 6

Toward clinical applications. (*a*) The frequency scatter plot of a coherent anti-Stokes Raman scattering (CARS) image from a rabbit atherosclerotic lesion, which can be used to distinguish the lipid-rich and protein-rich components in the image. The two axes correspond to CARS signal intensities at 2,850 cm^{-1} (CH$_2$ stretching) and 2,924 cm^{-1} (CH$_3$ stretching). (*b–d*) Reconstructed CARS images using frequency components 1–3 represented in panel *a*. (*e*) Bright field and (*f*) stimulated Raman scattering (SRS) images of the margin between human glioblastoma multiforme xenografts in a mouse brain and normal brain tissue. The contrast in the SRS image clearly highlights the tumor margin. Panels *a–d* and *e–f* adapted with permission from References 101 and 123, respectively.

multiforme. **Figure 6***e* shows a bright field image of the tumor margin, in which no features can be used to help distinguish the tumor. The corresponding two-color SRS image in **Figure 6***f* clearly shows a tumor margin, which is marked by the boundary between the protein-rich and lipid-rich tissues. Many human internal organs can be reached by light with the assistance of endoscopy. Incorporating CRS microscopy into endoscopy could significantly extend its in vivo applications for diagnosing disease in, for example, the gastrointestinal tract, urinary tract, or reproductive system. Nonlinear optical microscopy, such as MPF or SHG, has been integrated with endoscopy to perform ex vivo imaging of mouse lung and colon (178), as well as the collagen fiber morphology of mouse cervix (179), thus paving the way for further in vivo study. Proof-of-principle CRS endomicroscopy has also been reported (180, 181). CRS-based fiber-bundle probes have also been developed for endoscopic use (182).

8. OUTLOOK

Looking into the future, we expect to see the growth of CRS imaging through pioneering work in several directions. First, the shift from the C–H stretching region (2,800–3,100 cm^{-1}) to the fingerprint region (500–1,800 cm^{-1}) is an important step forward because the rich chemical information in the fingerprint region may allow visualization of a broader range of molecules in biology. Although the CRS signal level is sometimes weaker in the fingerprint region when compared with that in the C–H stretching region, outstanding work has shown the possibility of using fingerprint vibrational bonds, such as C=O, C=C, and S=O, for CRS imaging, as mentioned in

Section 4. Additionally, the attempt to separate the crowded and overlapping vibrational spectra in the fingerprint region has given rise to various hyperspectral CRS microscopy techniques that are equipped with advanced methods of data analysis, as reviewed in Section 3. Further work in the fingerprint region is expected to light up new endogenous biomarkers that can be used for biomedical purposes.

Second, another important trend is the development and application of exogenous Raman probes, as discussed in Section 4.2. These Raman probes are usually much smaller than fluorescence labels and, therefore, can be used to label small biomolecules and to reduce the perturbation introduced into a biological system while simultaneously providing remarkable contrast. The invention of new Raman tags could further extend the frontier of CRS microscopy in biology.

The development of hyperspectral CRS microscopy introduces the possibility of fast Raman spectral collection on a microsecond scale, which was theoretically predicted (see Sections 2.3 and 2.4). Currently, the CCD readout rate is the major factor limiting millisecond spectral collection in CARS (34). The Cheng group (83) recently developed multiplex SRS microscopy capable of collecting a Raman spectrum in 32 μs at each pixel. This significant improvement in spectral-collection speed could open new possibilities for CRS microscopy, such as tracking fast biological dynamics and developing CRS-based flow cytometry for high-throughput analysis of single cells.

Incorporating CRS microscopy into endoscopy could provide better diagnosis of diseases in the human gastrointestinal, urinary, and reproductive systems. Fiber laser sources will play an increasingly important part in the development of clinical CRS systems. Although CRS endoscopy is still in the early stages of development for use as an in vivo diagnostic tool, extensive efforts will ultimately lead to versatile and valuable CRS tools for clinical use. In conclusion, we expect that the vibrational imaging field will be propelled by CRS microscopy and that the enrichment of scientific and clinical knowledge will be driven by rapid, in vivo CRS imaging.

SUMMARY POINTS

1. Coherent Raman scattering (CRS) microscopy's signal level is much higher than that of spontaneous Raman microscopy; thus, it allows label-free chemical imaging of biological samples that is as fast as fluorescence microscopy.

2. The signal-to-noise ratio in spontaneous Raman and CRS imaging is determined by the signal level and three major noise sources: shot noise, laser relative intensity $1/f$ noise, and detector Johnson noise.

3. By using multivariate analysis to distinguish overlapping Raman bands, hyperspectral CRS microscopy can provide concentration maps of different chemical components in a specimen.

4. The CRS microscope offers a versatile platform for implementing multimodal non-linear optical microscopy, which is capable of providing both structural and chemical measurements.

5. Fiber lasers are expected to play an important part in reducing the cost and size of CRS microscopy systems.

6. Clinical applications of CRS microscopy are still in the early stages of development. Incorporating CRS microscopy into various clinical apparatuses, such as endoscopy systems, would significantly increase its clinical value.

DISCLOSURE STATEMENT

The authors are not aware of any affiliations, memberships, funding, or financial holdings that might be perceived as affecting the objectivity of this review.

ACKNOWLEDGMENTS

LITERATURE CITED

1. Raman CV, Krishnan KS. 1928. A new type of secondary radiation. *Nature* 121:501–2
2. Hendra PJ, Stratton PM. 1969. Laser-Raman spectroscopy. *Chem. Rev.* 69:325–44
3. Delhaye M, Dhamelincourt P. 1975. Raman microprobe and microscope with laser excitation. *J. Raman Spectrosc.* 3:33–43
4. Abraham J, Etz E. 1979. Molecular microanalysis of pathological specimens in situ with a laser-Raman microprobe. *Science* 206:716–18
5. Palonpon AF, Ando J, Yamakoshi H, Dodo K, Sodeoka M, et al. 2013. Raman and SERS microscopy for molecular imaging of live cells. *Nat. Protoc.* 8:677–92
6. Yamakoshi H, Dodo K, Okada M, Ando J, Palonpon A, et al. 2011. Imaging of EdU, an alkyne-tagged cell proliferation probe, by Raman microscopy. *J. Am. Chem. Soc.* 133:6102–5
7. Cheng J-X, Xie XS. 2012. *Coherent Raman Scattering Microscopy*. London: CRC
8. Boyd RW. 2003. *Nonlinear Optics*. Burlington, MA: Academic. 2nd ed.
9. Cheng J-X, Xie XS. 2003. Coherent anti-Stokes Raman scattering microscopy: instrumentation, theory, and applications. *J. Phys. Chem. B* 108:827–40
10. Terhune RW, Maker PD, Savage CM. 1965. Measurements of nonlinear light scattering. *Phys. Rev. Lett.* 14:681–84
11. Régnier PR, Taran JPE. 1973. On the possibility of measuring gas concentrations by stimulated anti-Stokes scattering. *Appl. Phys. Lett.* 23:240–42
12. Gord JR, Meyer TR, Roy S. 2008. Applications of ultrafast lasers for optical measurements in combusting flows. *Annu. Rev. Anal. Chem.* 1:663–87
13. Duncan MD, Reintjes J, Manuccia TJ. 1982. Scanning coherent anti-Stokes Raman microscope. *Opt. Lett.* 7:350–52
14. Zumbusch A, Holtom GR, Xie XS. 1999. Three-dimensional vibrational imaging by coherent anti-Stokes Raman scattering. *Phys. Rev. Lett.* 82:4142–45
15. Cheng J-X, Book LD, Xie XS. 2001. Polarization coherent anti-Stokes Raman scattering microscopy. *Opt. Lett.* 26:1341–43
16. Cheng J-X, Jia YK, Zheng G, Xie XS. 2002. Laser-scanning coherent anti-Stokes Raman scattering microscopy and applications to cell biology. *Biophys. J.* 83:502–9
17. Volkmer A, Cheng J-X, Sunney Xie X. 2001. Vibrational imaging with high sensitivity via epidetected coherent anti-Stokes Raman scattering microscopy. *Phys. Rev. Lett.* 87:023901
18. Evans CL, Potma EO, Puoris'haag M, Côté D, Lin CP, Xie XS. 2005. Chemical imaging of tissue in vivo with video-rate coherent anti-Stokes Raman scattering microscopy. *PNAS* 102:16807–12
19. Cheng J-X, Volkmer A, Xie XS. 2002. Theoretical and experimental characterization of coherent anti-Stokes Raman scattering microscopy. *J. Opt. Soc. Am. B* 19:1363–75
20. Cheng J-X, Volkmer A, Book LD, Xie XS. 2002. Multiplex coherent anti-Stokes Raman scattering microspectroscopy and study of lipid vesicles. *J. Phys. Chem. B* 106:8493–98
21. Müller M, Schins JM. 2002. Imaging the thermodynamic state of lipid membranes with multiplex CARS microscopy. *J. Phys. Chem. B* 106:3715–23

22. Rinia HA, Bonn M, Müller M. 2006. Quantitative multiplex CARS spectroscopy in congested spectral regions. *J. Phys. Chem. B* 110:4472–79

23. Kee TW, Zhao H, Cicerone MT. 2006. One-laser interferometric broadband coherent anti-Stokes Raman scattering. *Opt. Express* 14:3631–40

24. Nan X, Cheng J-X, Xie XS. 2003. Vibrational imaging of lipid droplets in live fibroblast cells with coherent anti-Stokes Raman scattering microscopy. *J. Lipid Res.* 44:2202–8

25. Rinia HA, Burger KNJ, Bonn M, Müller M. 2008. Quantitative label-free imaging of lipid composition and packing of individual cellular lipid droplets using multiplex CARS microscopy. *Biophys. J.* 95:4908–14

26. Wang H, Fu Y, Zickmund P, Shi R, Cheng J-X. 2005. Coherent anti-stokes Raman scattering imaging of axonal myelin in live spinal tissues. *Biophys. J.* 89:581–91

27. Bélanger E, Henry FP, Vallée R, Randolph MA, Kochevar IE, et al. 2011. In vivo evaluation of demyelination and remyelination in a nerve crush injury model. *Biomed. Opt. Express* 2:2698–708

28. Shi Y, Zhang D, Huff TB, Wang X, Shi R, et al. 2011. Longitudinal in vivo coherent anti-Stokes Raman scattering imaging of demyelination and remyelination in injured spinal cord. *J. Biomed. Opt.* 16:1060121

29. Cheng J-X. 2007. Coherent anti-Stokes Raman scattering microscopy. *Appl. Spectrosc.* 61:197–208

30. Müller M, Zumbusch A. 2007. Coherent anti-Stokes Raman scattering microscopy. *ChemPhysChem* 8:2156–70

31. Evans CL, Xie XS. 2008. Coherent anti-Stokes Raman scattering microscopy: chemical imaging for biology and medicine. *Annu. Rev. Anal. Chem.* 1:883–909

32. Zumbusch A, Langbein W, Borri P. 2013. Nonlinear vibrational microscopy applied to lipid biology. *Prog. Lipid Res.* 52:615–32

33. Parekh SH, Lee YJ, Aamer KA, Cicerone MT. 2010. Label-free cellular imaging by broadband coherent anti-Stokes Raman scattering microscopy. *Biophys. J.* 99:2695–704

34. Camp CH Jr, Lee YJ, Heddleston JM, Hartshorn CM, Hight Walker AR, et al. 2014. High-speed coherent Raman fingerprint imaging of biological tissues. *Nat. Photonics* 8:627–34

35. Di Napoli C, Pope I, Masia F, Watson P, Langbein W, Borri P. 2014. Hyperspectral and differential CARS microscopy for quantitative chemical imaging in human adipocytes. *Biomed. Opt. Express* 5:1378–90

36. Pegoraro AF, Slepkov AD, Ridsdale A, Moffatt DJ, Stolow A. 2014. Hyperspectral multimodal CARS microscopy in the fingerprint region. *J. Biophotonics* 7:49–58

37. Woodbury EJ, Ng WK. 1962. Ruby operation in the near IR. *Proc. Inst. Radio Eng.* 50:2367

38. Ploetz E, Laimgruber S, Berner S, Zinth W, Gilch P. 2007. Femtosecond stimulated Raman microscopy. *Appl. Phys. B* 87:389–93

39. Freudiger CW, Min W, Saar BG, Lu S, Holtom GR, et al. 2008. Label-free biomedical imaging with high sensitivity by stimulated Raman scattering microscopy. *Science* 322:1857–61

40. Ozeki Y, Dake F, Kajiyama Si, Fukui K, Itoh K. 2009. Analysis and experimental assessment of the sensitivity of stimulated Raman scattering microscopy. *Opt. Express* 17:3651–58

41. Nandakumar P, Kovalev A, Volkmer A. 2009. Vibrational imaging based on stimulated Raman scattering microscopy. *New J. Phys.* 11:033026

42. Zhang D, Slipchenko MN, Cheng J-X. 2011. Highly sensitive vibrational imaging by femtosecond pulse stimulated Raman loss. *J. Phys. Chem. Lett.* 2:1248–53

43. Andresen ER, Berto P, Rigneault H. 2011. Stimulated Raman scattering microscopy by spectral focusing and fiber-generated soliton as Stokes pulse. *Opt. Lett.* 36:2387–89

44. Beier HT, Noojin GD, Rockwell BA. 2011. Stimulated Raman scattering using a single femtosecond oscillator with flexibility for imaging and spectral applications. *Opt. Express* 19:18885–92

45. Ozeki Y, Umemura W, Sumimura K, Nishizawa N, Fukui K, Itoh K. 2012. Stimulated Raman hyperspectral imaging based on spectral filtering of broadband fiber laser pulses. *Opt. Lett.* 37:431–33

46. Suhalim JL, Chung C-Y, Lilledahl MB, Lim RS, Levi M, et al. 2012. Characterization of cholesterol crystals in atherosclerotic plaques using stimulated Raman scattering and second-harmonic generation microscopy. *Biophys. J.* 102:1988–95

47. Fu D, Holtom G, Freudiger C, Zhang X, Xie XS. 2012. Hyperspectral imaging with stimulated Raman scattering by chirped femtosecond lasers. *J. Phys. Chem. B* 117:4634–40

48. Zhang D, Wang P, Slipchenko MN, Ben-Amotz D, Weiner AM, Cheng J-X. 2012. Quantitative vibrational imaging by hyperspectral stimulated Raman scattering microscopy and multivariate curve resolution analysis. *Anal. Chem.* 85:98–106

49. Zhang D, Wang P, Slipchenko MN, Cheng J-X. 2014. Fast vibrational imaging of single cells and tissues by stimulated Raman scattering microscopy. *Acc. Chem. Res.* 47:2282–90

50. Min W, Freudiger CW, Lu S, Xie XS. 2011. Coherent nonlinear optical imaging: beyond fluorescence microscopy. *Annu. Rev. Phys. Chem.* 62:507–30

51. Beenakker C, Büttiker M. 1992. Suppression of shot noise in metallic diffusive conductors. *Phys. Rev. B* 46:1889

52. Nyquist H. 1928. Thermal agitation of electric charge in conductors. *Phys. Rev.* 32:110–13

53. Kato Y, Takuma H. 1971. Absolute measurement of Raman-scattering cross sections of liquids. *J. Opt. Soc. Am.* 61:347–50

54. Chung C-Y, Boik J, Potma EO. 2013. Biomolecular imaging with coherent nonlinear vibrational microscopy. *Annu. Rev. Phys. Chem.* 64:77–99

55. Saar BG, Freudiger CW, Reichman J, Stanley CM, Holtom GR, Xie XS. 2010. Video-rate molecular imaging in vivo with stimulated Raman scattering. *Science* 330:1368–70

56. Dudovich N, Oron D, Silberberg Y. 2002. Single-pulse coherently controlled nonlinear Raman spectroscopy and microscopy. *Nature* 418:512–14

57. Bremer MT, Dantus M. 2013. Standoff explosives trace detection and imaging by selective stimulated Raman scattering. *Appl. Phys. Lett.* 103:061119

58. Heinrich C, Bernet S, Ritsch-Marte M. 2004. Wide-field coherent anti-Stokes Raman scattering microscopy. *Appl. Phys. Lett.* 84:816–18

59. Cheng J-X, Volkmer A, Book LD, Xie XS. 2001. An epi-detected coherent anti-Stokes Raman scattering (E-CARS) microscope with high spectral resolution and high sensitivity. *J. Phys. Chem. B* 105:1277–80

60. Ganikhanov F, Carrasco S, Sunney Xie X, Katz M, Seitz W, Kopf D. 2006. Broadly tunable dual-wavelength light source for coherent anti-Stokes Raman scattering microscopy. *Opt. Lett.* 31:1292–94

61. Bonn M, Müller M, Rinia HA, Burger KNJ. 2009. Imaging of chemical and physical state of individual cellular lipid droplets using multiplex CARS microscopy. *J. Raman Spectrosc.* 40:763–69

62. Bégin S, Burgoyne B, Mercier V, Villeneuve A, Vallée R, Côté D. 2011. Coherent anti-Stokes Raman scattering hyperspectral tissue imaging with a wavelength-swept system. *Biomed. Opt. Express* 2:1296–306

63. Garbacik ET, Herek JL, Otto C, Offerhaus HL. 2012. Rapid identification of heterogeneous mixture components with hyperspectral coherent anti-Stokes Raman scattering imaging. *J. Raman Spectrosc.* 43:651–55

64. Hellerer T, Enejder AMK, Zumbusch A. 2004. Spectral focusing: high spectral resolution spectroscopy with broad-bandwidth laser pulses. *Appl. Phys. Lett.* 85:25–27

65. Rocha-Mendoza I, Langbein W, Borri P. 2008. Coherent anti-Stokes Raman microspectroscopy using spectral focusing with glass dispersion. *Appl. Phys. Lett.* 93:201103

66. Langbein W, Rocha-Mendoza I, Borri P. 2009. Coherent anti-Stokes Raman micro-spectroscopy using spectral focusing: theory and experiment. *J. Raman Spectrosc.* 40:800–8

67. Pegoraro AF, Ridsdale A, Moffatt DJ, Jia Y, Pezacki JP, Stolow A. 2009. Optimally chirped multimodal CARS microscopy based on a single Ti:sapphire oscillator. *Opt. Express* 17:2984–96

68. Chen B-C, Sung J, Wu X, Lim S-H. 2011. Chemical imaging and microspectroscopy with spectral focusing coherent anti-Stokes Raman scattering. *J. Biomed. Opt.* 16:021112

69. Masia F, Glen A, Stephens P, Borri P, Langbein W. 2013. Quantitative chemical imaging and unsupervised analysis using hyperspectral coherent anti-Stokes Raman scattering microscopy. *Anal. Chem.* 85:10820–28

70. Volkmer A, Book LD, Xie XS. 2002. Time-resolved coherent anti-Stokes Raman scattering microscopy: imaging based on Raman free induction decay. *Appl. Phys. Lett.* 80:1505–7

71. Ogilvie JP, Beaurepaire E, Alexandrou A, Joffre M. 2006. Fourier-transform coherent anti-Stokes Raman scattering microscopy. *Opt. Lett.* 31:480–82

72. Vartiainen EM, Rinia HA, Müller M, Bonn M. 2006. Direct extraction of Raman line-shapes from congested CARS spectra. *Opt. Express* 14:3622–30

73. Liu Y, Lee YJ, Cicerone MT. 2009. Broadband CARS spectral phase retrieval using a time-domain Kramers–Kronig transform. *Opt. Lett.* 34:1363–65

74. Marks DL, Boppart SA. 2004. Nonlinear interferometric vibrational imaging. *Phys. Rev. Lett.* 92:123905

75. Slipchenko MN, Oglesbee RA, Zhang D, Wu W, Cheng J-X. 2012. Heterodyne detected nonlinear optical imaging in a lock-in free manner. *J. Biophotonics* 5:801–7

76. Wang K, Zhang D, Charan K, Slipchenko MN, Wang P, et al. 2013. Time-lens based hyperspectral stimulated Raman scattering imaging and quantitative spectral analysis. *J. Biophotonics* 6:815–20

77. Wang P, Li J, Wang P, Hu CR, Zhang D, et al. 2013. Label-free quantitative imaging of cholesterol in intact tissues by hyperspectral stimulated Raman scattering microscopy. *Angew. Chem. Int. Ed.* 52:13042–46

78. Fu D, Zhou J, Zhu WS, Manley PW, Wang YK, et al. 2014. Imaging the intracellular distribution of tyrosine kinase inhibitors in living cells with quantitative hyperspectral stimulated Raman scattering. *Nat. Chem.* 6:614–22

79. Fu D, Lu F-K, Zhang X, Freudiger C, Pernik DR, et al. 2012. Quantitative chemical imaging with multiplex stimulated Raman scattering microscopy. *J. Am. Chem. Soc.* 134:3623–26

80. Marx B, Czerwinski L, Light R, Somekh M, Gilch P. 2014. Multichannel detectors for femtosecond stimulated Raman microscopy—ideal and real ones. *J. Raman Spectrosc.* 45:521–27

81. Rock W, Bonn M, Parekh SH. 2013. Near shot-noise limited hyperspectral stimulated Raman scattering spectroscopy using low energy lasers and a fast CMOS array. *Opt. Express* 21:15113–20

82. Seto K, Okuda Y, Tokunaga E, Kobayashi T. 2013. Development of a multiplex stimulated Raman microscope for spectral imaging through multi-channel lock-in detection. *Rev. Sci. Instrum.* 84:083705

83. Liao C-S, Slipchenko MN, Wang P, Li J, Lee S-Y, et al. 2015. Microsecond scale vibrational spectroscopic imaging by multiplex stimulated Raman scattering microscopy. *Light Sci. Appl.* 4:e265

84. Le TT, Yue S, Cheng J-X. 2010. Shedding new light on lipid biology with coherent anti-Stokes Raman scattering microscopy. *J. Lipid Res.* 51:3091–102

85. Yue S, Slipchenko MN, Cheng J-X. 2011. Multimodal nonlinear optical microscopy. *Laser Photonics Rev.* 5:496–512

86. Pezacki JP, Blake JA, Danielson DC, Kennedy DC, Lyn RK, Singaravelu R. 2011. Chemical contrast for imaging living systems: molecular vibrations drive CARS microscopy. *Nat. Chem. Biol.* 7:137–45

87. Suhalim JL, Boik JC, Tromberg BJ, Potma EO. 2012. The need for speed. *J. Biophotonics* 5:387–95

88. Paar M, Jüngst C, Steiner NA, Magnes C, Sinner F, et al. 2012. Remodeling of lipid droplets during lipolysis and growth in adipocytes. *J. Biol. Chem.* 287:11164–73

89. Fussell A, Garbacik E, Offerhaus H, Kleinebudde P, Strachan C. 2013. In situ dissolution analysis using coherent anti-Stokes Raman scattering (CARS) and hyperspectral CARS microscopy. *Eur. J. Pharm. Biopharm.* 85:1141–47

90. Le TT, Huff TB, Cheng J-X. 2009. Coherent anti-Stokes Raman scattering imaging of lipids in cancer metastasis. *BMC Cancer* 9:42

91. Mitra R, Chao O, Urasaki Y, Goodman OB, Le TT. 2012. Detection of lipid-rich prostate circulating tumour cells with coherent anti-Stokes Raman scattering microscopy. *BMC Cancer* 12:540

92. Okuno M, Kano H, Fujii K, Bito K, Naito S, et al. 2014. Surfactant uptake dynamics in mammalian cells elucidated with quantitative coherent anti-Stokes Raman scattering microspectroscopy. *PLOS ONE* 9:e93401

93. Hellerer T, Axäng C, Brackmann C, Hillertz P, Pilon M, Enejder A. 2007. Monitoring of lipid storage in *Caenorhabditis elegans* using coherent anti-Stokes Raman scattering (CARS) microscopy. *PNAS* 104:14658–63

94. Yen K, Le TT, Bansal A, Narasimhan SD, Cheng J-X, Tissenbaum HA. 2010. A comparative study of fat storage quantitation in nematode *Caenorhabditis elegans* using label and label-free methods. *PLOS ONE* 5:e12810

95. Le TT, Duren HM, Slipchenko MN, Hu C-D, Cheng J-X. 2010. Label-free quantitative analysis of lipid metabolism in living *Caenorhabditis elegans*. *J. Lipid Res.* 51:672–77

96. Fu Y, Wang H, Huff TB, Shi R, Cheng J-X. 2007. Coherent anti-Stokes Raman scattering imaging of myelin degradation reveals a calcium-dependent pathway in Lyso-PtdCho-induced demyelination. *J. Neurosci. Res.* 85:2870–81

97. Shi Y, Kim S, Huff TB, Borgens RB, Park K, et al. 2010. Effective repair of traumatically injured spinal cord by nanoscale block copolymer micelles. *Nat. Nanotechnol.* 5:80–87

98. Huff TB, Cheng J-X. 2007. In vivo coherent anti-Stokes Raman scattering imaging of sciatic nerve tissue. *J. Microsc.* 225:175–82

99. Jung Y, Ng JH, Keating CP, Senthil-Kumar P, Zhao J, et al. 2014. Comprehensive evaluation of peripheral nerve regeneration in the acute healing phase using tissue clearing and optical microscopy in a rodent model. *PLOS ONE* 9:e94054

100. Lim RS, Suhalim JL, Miyazaki-Anzai S, Miyazaki M, Levi M, et al. 2011. Identification of cholesterol crystals in plaques of atherosclerotic mice using hyperspectral CARS imaging. *J. Lipid Res.* 52:2177–86

101. Meyer T, Chemnitz M, Baumgartl M, Gottschall T, Pascher TR, et al. 2013. Expanding multimodal microscopy by high spectral resolution coherent anti-Stokes Raman scattering imaging for clinical disease diagnostics. *Anal. Chem.* 85:6703–15

102. Breunig HG, Weinigel M, Bückle R, Kellner-Höfer M, Lademann J, et al. 2013. Clinical coherent anti-Stokes Raman scattering and multiphoton tomography of human skin with a femtosecond laser and photonic crystal fiber. *Laser Phys. Lett.* 10:025604

103. Galli R, Uckermann O, Koch E, Schackert G, Kirsch M, Steiner G. 2014. Effects of tissue fixation on coherent anti-Stokes Raman scattering images of brain. *J. Biomed. Opt.* 19:071402

104. Cheng J-X, Pautot S, Weitz DA, Xie XS. 2003. Ordering of water molecules between phospholipid bilayers visualized by coherent anti-Stokes Raman scattering microscopy. *PNAS* 100:9826–30

105. Zimmerley M, Younger R, Valenton T, Oertel DC, Ward JL, Potma EO. 2010. Molecular orientation in dry and hydrated cellulose fibers: a coherent anti-Stokes Raman scattering microscopy study. *J. Phys. Chem. B* 114:10200–8

106. Kennedy AP, Sutcliffe J, Cheng J-X. 2005. Molecular composition and orientation in myelin figures characterized by coherent anti-Stokes Raman scattering microscopy. *Langmuir* 21:6478–86

107. de Vito G, Bifone A, Piazza V. 2012. Rotating-polarization CARS microscopy: combining chemical and molecular orientation sensitivity. *Opt. Express* 20:29369–77

108. Dou W, Zhang D, Jung Y, Cheng J-X, Umulis DM. 2012. Label-free imaging of lipid-droplet intracellular motion in early *Drosophila* embryos using femtosecond-stimulated Raman loss microscopy. *Biophys. J.* 102:1666–75

109. Wang MC, Min W, Freudiger CW, Ruvkun G, Xie XS. 2011. RNAi screening for fat regulatory genes with SRS microscopy. *Nat. Methods* 8:135–38

110. Zhang X, Roeffaers MBJ, Basu S, Daniele JR, Fu D, et al. 2012. Label-free live-cell imaging of nucleic acids using stimulated Raman scattering microscopy. *ChemPhysChem* 13:1054–59

111. Saar BG, Zeng Y, Freudiger CW, Liu Y-S, Himmel ME, et al. 2010. Label-free, real-time monitoring of biomass processing with stimulated Raman scattering microscopy. *Angew. Chem. Int. Ed.* 49:5476–79

112. Wei L, Yu Y, Shen Y, Wang MC, Min W. 2013. Vibrational imaging of newly synthesized proteins in live cells by stimulated Raman scattering microscopy. *PNAS* 110:11226–31

113. Wei L, Hu F, Shen Y, Chen Z, Yu Y, et al. 2014. Live-cell imaging of alkyne-tagged small biomolecules by stimulated Raman scattering. *Nat. Methods* 11:410–12

114. Hong S, Chen T, Zhu Y, Li A, Huang Y, Chen X. 2014. Live-cell stimulated Raman scattering imaging of alkyne-tagged biomolecules. *Angew. Chem. Int. Ed.* 126:5937–41

115. Shen Y, Xu F, Wei L, Hu F, Min W. 2014. Live-cell quantitative imaging of proteome degradation by stimulated Raman scattering. *Angew. Chem. Int. Ed.* 53:5596–99

116. Hu F, Wei L, Zheng C, Shen Y, Min W. 2014. Live-cell vibrational imaging of choline metabolites by stimulated Raman scattering coupled with isotope-based metabolic labeling. *Analyst* 139:2312–17

117. Wei L, Shen Y, Xu F, Hu F, Harrington JK, et al. 2015. Imaging complex protein metabolism in live organisms by stimulated Raman scattering microscopy with isotope labeling. *ACS Chem. Biol.* 10:901–8

118. Chen Z, Paley DW, Wei L, Weisman AL, Friesner RA, et al. 2014. Multicolor live-cell chemical imaging by isotopically edited alkyne vibrational palette. *J. Am. Chem. Soc.* 136:8027–33

119. Lee HJ, Zhang W, Zhang D, Yang Y, Liu B, et al. 2015. Assessing cholesterol storage in live cells and *C. elegans* by stimulated Raman scattering imaging of phenyl-diyne cholesterol. *Sci. Rep.* 5:7930

120. Hu C-R, Zhang D, Slipchenko MN, Cheng J-X, Hu B. 2014. Label-free real-time imaging of myelination in the *Xenopus laevis* tadpole by in vivo stimulated Raman scattering microscopy. *J. Biomed. Opt.* 19:086005

121. Wang P, Liu B, Zhang D, Belew MY, Tissenbaum HA, Cheng J-X. 2014. Imaging lipid metabolism in live *Caenorhabditis elegans* using fingerprint vibrations. *Angew. Chem. Int. Ed.* 53:11787–92

122. Yue S, Li J, Lee S-Y, Lee HJ, Shao T, et al. 2014. Cholesteryl ester accumulation induced by PTEN loss and PI3K/AKT activation underlies human prostate cancer aggressiveness. *Cell Metab.* 19:393–406

123. Ji M, Orringer DA, Freudiger CW, Ramkissoon S, Liu X, et al. 2013. Rapid, label-free detection of brain tumors with stimulated Raman scattering microscopy. *Sci. Transl. Med.* 5:201ra119

124. Freudiger CW, Pfannl R, Orringer DA, Saar BG, Ji M, et al. 2012. Multicolored stain-free histopathology with coherent Raman imaging. *Lab. Investig.* 92:1492–502

125. Huff TB, Shi Y, Fu Y, Wang H, Cheng J-X. 2008. Multimodal nonlinear optical microscopy and applications to central nervous system imaging. *IEEE J. Sel. Top. Quantum Electron.* 14:4–9

126. Chen H, Wang H, Slipchenko MN, Jung Y, Shi Y, et al. 2009. A multimodal platform for nonlinear optical microscopy and microspectroscopy. *Opt. Express* 17:1282–90

127. Zhai Y-H, Goulart C, Sharping JE, Wei H, Chen S, et al. 2011. Multimodal coherent anti-Stokes Raman spectroscopic imaging with a fiber optical parametric oscillator. *Appl. Phys. Lett.* 98:191106

128. Meyer T, Baumgartl M, Gottschall T, Pascher T, Wuttig A, et al. 2013. A compact microscope setup for multimodal nonlinear imaging in clinics and its application to disease diagnostics. *Analyst* 138:4048–57

129. Le TT, Rehrer CW, Huff TB, Nichols MB, Camarillo IG, Cheng J-X. 2007. Nonlinear optical imaging to evaluate the impact of obesity on mammary gland and tumor stroma. *Mol. Imaging* 6:205

130. Wang H-W, Langohr IM, Sturek M, Cheng J-X. 2009. Imaging and quantitative analysis of atherosclerotic lesions by CARS-based multimodal nonlinear optical microscopy. *Arterioscler. Thromb. Vasc. Biol.* 29:1342–48

131. Mansfield J, Yu J, Attenburrow D, Moger J, Tirlapur U, et al. 2009. The elastin network: its relationship with collagen and cells in articular cartilage as visualized by multiphoton microscopy. *J. Anat.* 215:682–91

132. Vogler N, Medyukhina A, Latka I, Kemper S, Böhm M, et al. 2011. Towards multimodal nonlinear optical tomography—experimental methodology. *Laser Phys. Lett.* 8:617–24

133. Mouras R, Bagnaninchi PO, Downes AR, Elfick AP. 2012. Label-free assessment of adipose-derived stem cell differentiation using coherent anti-Stokes Raman scattering and multiphoton microscopy. *J. Biomed. Opt.* 17:116011

134. Mortati L, Divieto C, Sassi MP. 2012. CARS and SHG microscopy to follow collagen production in living human corneal fibroblasts and mesenchymal stem cells in fibrin hydrogel 3D cultures. *J. Raman Spectrosc.* 43:675–80

135. Segawa H, Okuno M, Kano H, Leproux P, Couderc V, Hamaguchi H-O. 2012. Label-free tetra-modal molecular imaging of living cells with CARS, SHG, THG and TSFG (coherent anti-Stokes Raman scattering, second harmonic generation, third harmonic generation and third-order sum frequency generation). *Opt. Express* 20:9551–57

136. Garrett NL, Lalatsa A, Uchegbu I, Schätzlein A, Moger J. 2012. Exploring uptake mechanisms of oral nanomedicines using multimodal nonlinear optical microscopy. *J. Biophotonics* 5:458–68

137. Hoover EE, Squier JA. 2013. Advances in multiphoton microscopy technology. *Nat. Photonics* 7:93–101

138. Jung Y, Slipchenko MN, Liu CH, Ribbe AE, Zhong Z, et al. 2010. Fast detection of the metallic state of individual single-walled carbon nanotubes using a transient-absorption optical microscope. *Phys. Rev. Lett.* 105:217401

139. Tong L, Liu Y, Dolash BD, Jung Y, Slipchenko MN, et al. 2012. Label-free imaging of semiconducting and metallic carbon nanotubes in cells and mice using transient absorption microscopy. *Nat. Nanotechnol.* 7:56–61

140. Wang H, Huff TB, Zweifel DA, He W, Low PS, et al. 2005. In vitro and in vivo two-photon luminescence imaging of single gold nanorods. *PNAS* 102:15752–56

141. Tong L, Cobley CM, Chen J, Xia Y, Cheng J-X. 2010. Bright three-photon luminescence from gold/silver alloyed nanostructures for bioimaging with negligible photothermal toxicity. *Angew. Chem. Int. Ed.* 49:3485–88

142. Kim H, Sheps T, Collins PG, Potma EO. 2009. Nonlinear optical imaging of individual carbon nanotubes with four-wave-mixing microscopy. *Nano Lett.* 9:2991–95

143. Min W, Lu S, Chong S, Roy R, Holtom GR, Xie XS. 2009. Imaging chromophores with undetectable fluorescence by stimulated emission microscopy. *Nature* 461:1105–9

144. Wei L, Min W. 2012. Pump-probe optical microscopy for imaging nonfluorescent chromophores. *Anal. Bioanal. Chem.* 403:2197–202

145. Min W, Lu S, Rueckel M, Holtom GR, Xie XS. 2009. Near-degenerate four-wave-mixing microscopy. *Nano Lett.* 9:2423–26

146. Lu S, Min W, Chong S, Holtom GR, Xie XS. 2010. Label-free imaging of heme proteins with two-photon excited photothermal lens microscopy. *Appl. Phys. Lett.* 96:113701

147. Moger J, Garrett N, Begley D, Mihoreanu L, Lalatsa A, et al. 2012. Imaging cortical vasculature with stimulated Raman scattering and two-photon photothermal lensing microscopy. *J. Raman Spectrosc.* 43:668–74

148. Slepkov AD, Ridsdale A, Wan H-N, Wang M-H, Pegoraro AF, et al. 2011. Forward-collected simultaneous fluorescence lifetime imaging and coherent anti-Stokes Raman scattering microscopy. *J. Biomed. Opt.* 16:021103

149. Slipchenko MN, Le TT, Chen H, Cheng J-X. 2009. High-speed vibrational imaging and spectral analysis of lipid bodies by compound Raman microscopy. *J. Phys. Chem. B* 113:7681–86

150. Slipchenko MN, Chen H, Ely DR, Jung Y, Carvajal MT, Cheng J-X. 2010. Vibrational imaging of tablets by epi-detected stimulated Raman scattering microscopy. *Analyst* 135:2613–19

151. Yue S, Cárdenas-Mora JM, Chaboub LS, Lelièvre SA, Cheng J-X. 2012. Label-free analysis of breast tissue polarity by Raman imaging of lipid phase. *Biophys. J.* 102:1215–23

152. Galli R, Uckermann O, Winterhalder MJ, Sitoci-Ficici KH, Geiger KD, et al. 2012. Vibrational spectroscopic imaging and multiphoton microscopy of spinal cord injury. *Anal. Chem.* 84:8707–14

153. Le TT, Ziemba A, Urasaki Y, Brotman S, Pizzorno G. 2012. Label-free evaluation of hepatic microvesicular steatosis with multimodal coherent anti-Stokes Raman scattering microscopy. *PLOS ONE* 7:e51092

154. Chong A, Renninger WH, Wise FW. 2007. All-normal-dispersion femtosecond fiber laser with pulse energy above 20 nJ. *Opt. Lett.* 32:2408–10

155. Kieu K, Renninger W, Chong A, Wise F. 2009. Sub-100 fs pulses at watt-level powers from a dissipative-soliton fiber laser. *Opt. Lett.* 34:593–95

156. Chichkov NB, Hapke C, Neumann J, Kracht D, Wandt D, Morgner U. 2012. Pulse duration and energy scaling of femtosecond all-normal dispersion fiber oscillators. *Opt. Express* 20:3844–52

157. Tang S, Liu J, Krasieva TB, Chen Z, Tromberg BJ. 2009. Developing compact multiphoton systems using femtosecond fiber lasers. *J. Biomed. Opt.* 14:030508

158. Nie B, Saytashev I, Chong A, Liu H, Arkhipov SN, et al. 2012. Multimodal microscopy with sub-30 fs Yb fiber laser oscillator. *Biomed. Opt. Express* 3:1750–56

159. Baumgartl M, Lecaplain C, Hideur A, Limpert J, Tünnermann A. 2012. 66 W average power from a microjoule-class sub-100 fs fiber oscillator. *Opt. Lett.* 37:1640–42

160. Paulsen HN, Hilligse KM, Thøgersen J, Keiding SR, Larsen JJ. 2003. Coherent anti-Stokes Raman scattering microscopy with a photonic crystal fiber based light source. *Opt. Lett.* 28:1123–25

161. Krauss G, Hanke T, Sell A, Träutlein D, Leitenstorfer A, et al. 2009. Compact coherent anti-Stokes Raman scattering microscope based on a picosecond two-color Er:fiber laser system. *Opt. Lett.* 34:2847–49

162. Lefrancois S, Fu D, Holtom GR, Kong L, Wadsworth WJ, et al. 2012. Fiber four-wave mixing source for coherent anti-Stokes Raman scattering microscopy. *Opt. Lett.* 37:1652–54

163. Lamb ES, Lefrancois S, Ji M, Wadsworth WJ, Sunney Xie X, Wise FW. 2013. Fiber optical parametric oscillator for coherent anti-Stokes Raman scattering microscopy. *Opt. Lett.* 38:4154–57

164. Nose K, Ozeki Y, Kishi T, Sumimura K, Nishizawa N, et al. 2012. Sensitivity enhancement of fiber-laser-based stimulated Raman scattering microscopy by collinear balanced detection technique. *Opt. Express* 20:13958–65

165. Nose K, Kishi T, Ozeki Y, Kanematsu Y, Takata H, et al. 2014. Stimulated Raman spectral microscope using synchronized Er-and Yb-fiber lasers. *Jpn. J. Appl. Phys.* 53:052401

166. Freudiger CW, Yang W, Holtom GR, Peyghambarian N, Xie XS, Kieu KQ. 2014. Stimulated Raman scattering microscopy with a robust fibre laser source. *Nat. Photonics* 8:153–59

167. Masihzadeh O, Ammar DA, Kahook MY, Lei TC. 2013. Coherent anti-Stokes Raman scattering (CARS) microscopy: a novel technique for imaging the retina. *Investig. Ophthalmol. Vis. Sci.* 54:3094–101

168. Wu Y-M, Chen H-C, Chang W-T, Jhan J-W, Lin H-L, Liau I. 2009. Quantitative assessment of hepatic fat of intact liver tissues with coherent anti-Stokes Raman scattering microscopy. *Anal. Chem.* 81:1496–504

169. Gao L, Zhou H, Thrall MJ, Li F, Yang Y, et al. 2011. Label-free high-resolution imaging of prostate glands and cavernous nerves using coherent anti-Stokes Raman scattering microscopy. *Biomed. Opt. Express* 2:915–26

170. Saar BG, Contreras-Rojas LR, Xie XS, Guy RH. 2011. Imaging drug delivery to skin with stimulated Raman scattering microscopy. *Mol. Pharm.* 8:969–75

171. Belsey NA, Garrett NL, Contreras-Rojas LR, Pickup-Gerlaugh AJ, Price GJ, et al. 2014. Evaluation of drug delivery to intact and porated skin by coherent Raman scattering and fluorescence microscopies. *J. Control. Release* 174:37–42

172. Breunig HG, Bückle R, Kellner-Höfer M, Weinigel M, Lademann J, et al. 2012. Combined in vivo multiphoton and CARS imaging of healthy and disease-affected human skin. *Microsc. Res. Tech.* 75:492–98

173. Zimmerley M, McClure RA, Choi B, Potma EO. 2009. Following dimethyl sulfoxide skin optical clearing dynamics with quantitative nonlinear multimodal microscopy. *Appl. Opt.* 48:D79–87

174. König K, Breunig H, Bückle R, Kellner-Höfer M, Weinigel M, et al. 2011. Optical skin biopsies by clinical CARS and multiphoton fluorescence/SHG tomography. *Laser Phys. Lett.* 8:465–68

175. Smith B, Naji M, Murugkar S, Alarcon E, Brideau C, et al. 2013. Portable, miniaturized, fibre delivered, multimodal CARS exoscope. *Opt. Express* 21:17161–75

176. Mittal R, Balu M, Krasieva T, Potma EO, Elkeeb L, et al. 2013. Evaluation of stimulated Raman scattering microscopy for identifying squamous cell carcinoma in human skin. *Laser Surg. Med.* 45:496–502

177. Drutis D, Hancewicz T, Pashkovski E, Feng L, Mihalov D, et al. 2014. Three-dimensional chemical imaging of skin using stimulated Raman scattering microscopy. *J. Biomed. Opt.* 19:111604

178. Rivera DR, Brown CM, Ouzounov DG, Pavlova I, Kobat D, et al. 2011. Compact and flexible raster scanning multiphoton endoscope capable of imaging unstained tissue. *PNAS* 108:17598–603

179. Zhang Y, Akins ML, Murari K, Xi J, Li M-J, et al. 2012. A compact fiber-optic SHG scanning endomicroscope and its application to visualize cervical remodeling during pregnancy. *PNAS* 109:12878–83

180. Légaré F, Evans CL, Ganikhanov F, Xie XS. 2006. Towards CARS endoscopy. *Opt. Express* 14:4427–32

181. Saar BG, Johnston RS, Freudiger CW, Xie XS, Seibel EJ. 2011. Coherent Raman scanning fiber endoscopy. *Opt. Lett.* 36:2396–98

182. Liu Z, Wang Z, Wang X, Xu X, Chen X, et al. 2013. Fiber bundle based probe with polarization for coherent anti-Stokes Raman scattering microendoscopy imaging. *Proc. SPIE* 8588:85880F. doi: 10.1117/12.2004229

ANNUAL REVIEWS
Connect With Our Experts
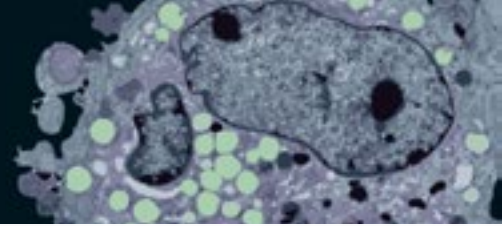
New From Annual Reviews:

Annual Review of Cancer Biology
cancerbio.annualreviews.org · Volume 1 · March 2017

ONLINE NOW!

Co-Editors: Tyler Jacks, *Massachusetts Institute of Technology*

Charles L. Sawyers, *Memorial Sloan Kettering Cancer Center*

The *Annual Review of Cancer Biology* reviews a range of subjects representing important and emerging areas in the field of cancer research. The *Annual Review of Cancer Biology* includes three broad themes: Cancer Cell Biology, Tumorigenesis and Cancer Progression, and Translational Cancer Science.

ANNUAL REVIEWS | CONNECT WITH OUR EXPERTS

650.493.4400/800.523.8635 (US/CAN)
www.annualreviews.org | service@annualreviews.org

Contents

Indexes

Errata

An online log of corrections to *Annual Review of Biomedical Engineering* articles may be
found at http://www.annualreviews.org/errata/bioeng